



**HAL**  
open science

## Linking ground-based data and satellite monitoring to understand the last two decades of eruptive activity at Sangay volcano, Ecuador

Francisco J. Vasconez, Silvana Hidalgo, Jean Battaglia, Stephen Hernandez, Benjamin Bernard, Diego Coppola, Sébastien Valade, Patricio Ramón, Santiago Arellano, Céline Liorzou, et al.

### ► To cite this version:

Francisco J. Vasconez, Silvana Hidalgo, Jean Battaglia, Stephen Hernandez, Benjamin Bernard, et al.. Linking ground-based data and satellite monitoring to understand the last two decades of eruptive activity at Sangay volcano, Ecuador. *Bulletin of Volcanology*, 2022, 84 (5), 10.1007/s00445-022-01560-w . insu-03684626

**HAL Id: insu-03684626**

**<https://insu.hal.science/insu-03684626v1>**

Submitted on 6 Dec 2022

**HAL** is a multi-disciplinary open access archive for the deposit and dissemination of scientific research documents, whether they are published or not. The documents may come from teaching and research institutions in France or abroad, or from public or private research centers.

L'archive ouverte pluridisciplinaire **HAL**, est destinée au dépôt et à la diffusion de documents scientifiques de niveau recherche, publiés ou non, émanant des établissements d'enseignement et de recherche français ou étrangers, des laboratoires publics ou privés.

# Linking ground-based data and satellite monitoring to understand the last two decades of eruptive activity at Sangay volcano, Ecuador

Francisco J. Vasconez<sup>1</sup>, Silvana Hidalgo<sup>1</sup>, Jean Battaglia<sup>2</sup>, Stephen Hernandez<sup>1</sup>, Benjamin Bernard<sup>1</sup>, Diego Coppola<sup>3</sup>, Sébastien Valade<sup>4</sup>, Patricio Ramón<sup>1</sup>, Santiago Arellano<sup>5</sup>, Céline Liorzou<sup>6</sup>, Marco Almeida<sup>1</sup>, Marcelo Ortíz<sup>1</sup>, Jorge Córdova<sup>1</sup>, Anais Vásconez Müller<sup>7</sup>.

<sup>1</sup> Instituto Geofísico de la Escuela Politécnica Nacional, Quito, Ecuador.

<sup>2</sup> Université Clermont Auvergne, CNRS, IRD, OPGC, Laboratoire Magmas et Volcans, Clermont-Ferrand, France.

<sup>3</sup> Dipartimento di Scienze della Terra – Università degli Studi di Torino, Torino, Italy.

<sup>4</sup> Instituto de Geofísica, Universidad Nacional Autónoma de México, Mexico City, Mexico.

<sup>5</sup> Department of Space, Earth and Environment, Chalmers University of Technology, Göteborg, Sweden

<sup>6</sup> Université de Bretagne Occidentale, Géosciences Océan IUEM, 29280 Plouzané, France.

<sup>7</sup> School of Earth Sciences, University of Bristol, Bristol, BS8 1RJ, UK

## Abstract

Sangay is one of the most active volcanoes in Ecuador, as it has been almost continuously erupting at least since the 17th century. However, because of its remote location and low associated risk to human population, little is known about its eruptions. Here we summarize Sangay's volcanic activity from January 2001 to May 2020, based on ground-based data, satellite-derived observations, and chemical analysis of its erupted products. During the analyzed period, Sangay's activity changed from continuous to episodic, as revealed by seismic, thermal and ash emission data. We identified three main eruptive periods: the first, from 2001 to 2013, extruded a cumulative volume of  $100 \pm 50$  million  $\text{m}^3$  of lava through long-lived activity; the second emitted  $54 \pm 27$  million  $\text{m}^3$  in four short-lived episodes, which occurred once every year from 2015 to 2018; and finally, a third period since 2019, which has continuous but fluctuating intensity, and shows a significant increase of the extruded lava volume ( $172 \pm 86$  million  $\text{m}^3$  until 31 May 2020). Our results show a marked change in the eruption frequency and a significant increase in average discharge rate over time, although surface activity remained similar, with lava flows, small explosions, and ash venting. We propose that three magmatic processes acted to explain the observed changes: between 2001 and 2013 the long-living low intensity eruptions were promoted by buoyancy, while since 2019 similar but more intense activity was triggered by mass injections. In contrast, the episodic activity in between probably resulted from volatile exsolution due to crystallization (second boiling). Transitions between these three regimes are presumably the result of varying mass inflow rates. Our results provide insights into eruptive style transitions commonly observed at volcanoes of intermediate composition, such as Sangay, over a time scale of several years.

**Keywords:** Sangay volcano, long-lasting activity, episodic eruptions, size of the eruptions, eruption frequency

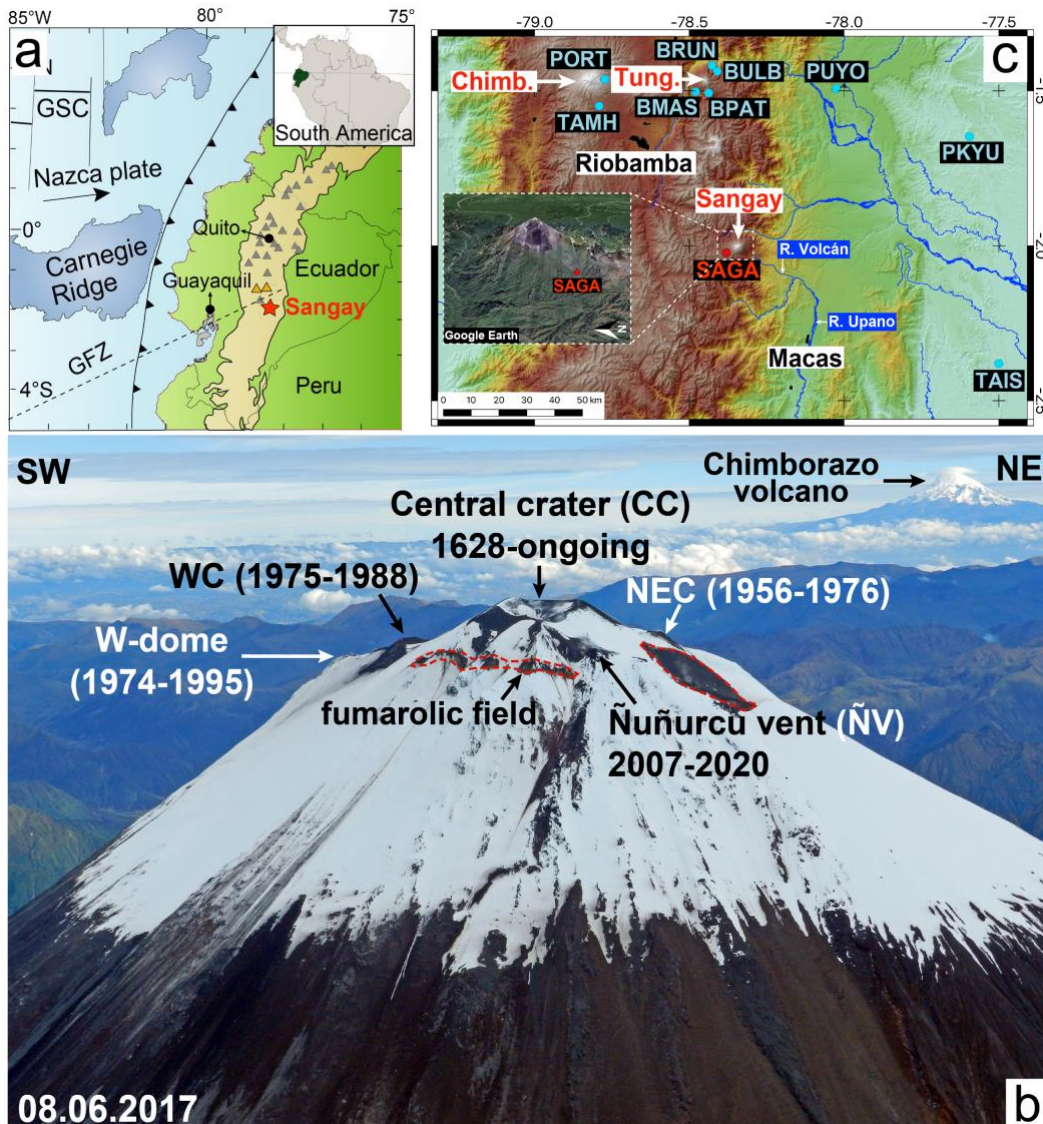
## Declarations:

[Data provided in Supplementary Material (SM-1, SM-2, and SM-3). No COI. Funding not applicable. FJV conceived of the project, conducted most of the analyses, performed all figures, and wrote the main manuscript. SH supervised the research and helped in the analysis and interpretation of the results and discussion. JB conducted the seismic and  $\text{SO}_2$  analyses at SAGA station. SHz carried out the regional seismic analysis. BB helped in the analysis of the results and discussion. DC provided the MIROVA data and helped in their analysis. SV provided de  $\text{SO}_2$  data and helped in their analysis. PR identified the change from long-lasting to episodic activity and helped in the analysis of thermal images. SA helped in the writing and discussion of the Sangay's model. CL performed the geochemical analysis of the ash samples. MA took and analyzed the thermal images. MO monitored seismic signals and superficial activity. JC took ash samples and maintained the remote SAGA station. AVM helped in the writing and discussion. All authors revised and enhanced the manuscript.]

54  
55  
56  
57  
58  
59  
60  
61  
62  
63  
64  
65  
66  
67  
68  
69  
70  
71  
72  
73  
74  
75

### 1. INTRODUCTION

Sangay (78.34°W; 2.00°S; 5326 m asl) is the southernmost active volcano of the Northern Volcanic Zone (NVZ) in the Andes (Fig. 1a). It lies in a remote area of the eastern flank of the Cordillera Real, within a rainforest with no car access and where rainy and cold weather conditions are prevalent during most of the year. Therefore, accessing the volcano is logistically difficult, giving way to only few direct observations. Sangay is a conical stratovolcano, which stands out by having a dome and three main craters at the summit area and a lateral vent, aligned west-east (Fig. 1b). According to Monzier et al. (1999) these vents evolved through time as follows: in 1628 A.D. there was only one Central Crater (CC) through which lava flows and eruptive plumes were emitted (Fig. 1b). This crater remains active until today. Later, in 1956, a new crater located to the Northeast (NEC) of the Central Crater was reported, and this remained active until 1976. During 1974 and 1975 two new vents also appeared at the western zone of the Central Crater: the West Crater (WC) and West dome (W-dome). The latter began as a fissure and became a lava dome in 1983. Activity of this dome claimed the life of two English explorers back in 1976 (Global Volcanism Program 1976). Finally, the Ñuñurcu vent (ÑV) is a lateral vent located to the southeast of the Central Crater from where in 2007 a lava dome/coulée was extruded. This vent was active until June 2020 and extruded lava flows down the southeastern flank of the edifice. Moreover, two large landslide scars account for the main morphology of Sangay volcano (Valverde et al. 2021). These scars and their associated debris avalanches occurred between 250-100 ka BP and 29 ka BP, respectively (Monzier et al. 1999; Valverde et al. 2021), and both affected the eastern and southeastern flanks leaving debris avalanche deposits where the city of Macas is now located with more than 24,400 inhabitants (Villareal 2017; Valverde et al. 2021, Fig. 1c).



76  
77  
78

Fig. 1 a) Main geodynamic features of Ecuador, which include Galápagos Spreading Center (GSC) and GFZ (Grijalva Fracture Zone); the red star shows the location of Sangay volcano, while Chimborazo and Tungurahua volcanoes and

79 the main cities are displayed as the orange triangles and the black dots, respectively. b) Aerial view of Sangay with its  
80 main features: West-dome (W-dome), West Crater (WC), Central Crater (CC), Ñuñurcu vent (ÑV) and Northeast  
81 Crater (NEC). The ages of the active vents are mainly based on [Monzier et al. \(1999\)](#). Chimborazo volcano is visible  
82 in the background. c) Location of the 10 broadband seismic stations used to detect Sangay seismicity, identifies with  
83 4-letter codes. SAGA station and the regional seismic network are pointed out as colored dots, while main rivers and  
84 cities are highlighted in blue and black, respectively. The location of Tungurahua, Chimborazo and Sangay volcanoes  
85 are also shown.

86  
87 Since 1628 A.D. eruptive activity at Sangay has been mostly of continuous nature ([Hall 1977](#)). The [Global  
88 Volcanism Program \(1996\)](#) reports eruptions from 1728 A.D. to 1916 A.D. and again since 1934 A.D.,  
89 seemingly more or less continuous. Based on historical records, in 1628, Riobamba city, located 50 km to  
90 the northwest of the volcano ([Fig. 1c](#)), was completely blanketed and darkened by ash for one and a half  
91 days, disrupting the daily life of the society of that epoch ([Monzier et al. 1999](#)). Additionally, over the last  
92 two decades and despite the almost continuous activity, on a few occasions has ash fallout affected large  
93 cities such as Guayaquil in 2018 and 2020, 170 km away from Sangay ([IGEPN 2018, 2020](#)). The low  
94 frequency of ash fallout reaching major cities is mainly due to the small height of the eruptive plumes, the  
95 low amount of ash and the remote location of the volcano. However, small communities sparsely located  
96 ~30-40 km to the west of the volcano, which is the prevalent direction of the winds ([Bernard et al. 2019](#)),  
97 have been affected by ash fallouts leading to the loss of crops and causing cattle diseases. Potential aviation  
98 hazards also exist given that the eruptive plumes and co-pyroclastic ash plumes could traverse air traffic  
99 routes near Sangay. Other phenomena like lava flows, pyroclastic density currents, and lahars are also  
100 common, but they are usually restricted to the volcanic ring plain (< 10 km away from the summit). All  
101 these phenomena were synthesized on the first hazard map published by [Ordoñez et al. \(2013\)](#). Finally,  
102 debris avalanches are possible to occur as Sangay grows higher and more unstable over time ([Monzier et  
103 al. 1999](#)).

104  
105 Throughout the years, only few scientific studies have been carried out on Sangay. [Johnson and Lees  
106 \(2000\)](#), [Konstantinou and Lin \(2004\)](#), and [Lees and Ruiz \(2008\)](#) explored seismic and acoustic signals of  
107 the degassing explosions at Sangay recorded in April 1998, based on a temporary experiment conducted at  
108 a close range from the summit (<2 km). They distinguished three types of explosive events: (1) simple  
109 impulses (<1 min in duration) generated by degassing explosions at the vent, (2) extended degassing  
110 ‘chugging’ events (1–5 Hz and duration of 2–5 min) which could be related to resonances in the conduit,  
111 and (3) extended degassing events (>5 Hz and >5 min). [Ortiz et al. \(2020\)](#) showed near-constant activity  
112 from mid 2006 to mid 2012, with eight detections per day on average for Sangay based on a temporary  
113 infrasound array. [Carn et al. \(2008\)](#) reported negligible SO<sub>2</sub> emissions at Sangay from 2004 to 2006 based  
114 on Total Ozone Mapping Spectrometer (TOMS) and Ozone Monitoring Instrument (OMI) satellite sensors.  
115 [Morales Rivera et al. \(2016\)](#) found consistent motion towards the satellite on the southwestern flank at  
116 1.3±0.4 cm/y and away on the southeastern flank at 4.3±0.4 cm/y based on ALOS Interferometric Synthetic  
117 Aperture Radar (InSAR) ground deformation surveys between 2007 and 2011. Given the satellite’s view  
118 direction, they suggested that the observed deformation was consistent with downhill motion of the steep  
119 flanks of the volcano by 3-5 cm/y.

120  
121 Furthermore, [Monzier et al. \(1999\)](#) performed an impressive field mission to collect samples from this  
122 remote volcano constructed over the last 500 ky. Interestingly, Sangay displays a particular geochemical  
123 signature when compared with the rest of the volcanoes in the Ecuadorian arc. They found Niobium-rich  
124 rocks and the most primitive basalt. In addition, the olivine-hosted melt inclusions analyzed from that basalt  
125 show high volatile (Sulfur-Chlorine-Fluorine) contents pleading for a volatile-enriched source for the  
126 magma ([Narvaez et al. 2018](#)). In a broader context, the magmatism in the southern termination of the  
127 Ecuadorian volcanic arc is the result of the partial melting of the mantle metasomatized by aqueous fluids  
128 released by an old and cold slab beneath the continental South American plate ([Fig. 1a, Monzier et al. 1999;  
129 Narvaez et al. 2018](#)).

130  
131 In this study, we used data from 10 permanent seismic stations, one of them coupled to an acoustic sensor  
132 and a ScanDOAS (Differential Optical Absorption Spectroscopy, [Fig. 1c](#)), instrument from the Network  
133 for Observation of Volcanic and Atmospheric Change (NOVAC). All these instruments were installed and  
134 are operated by the Instituto Geofísico (IG-EPN). This information is complemented by satellite  
135 observations to monitor the most recent eruptive activity of this remote volcano. The purpose of the present  
136 contribution is to address the lack of knowledge about Sangay’s volcanic activity by linking the available  
137 ground-based geophysical data and the satellite imagery of the last two decades. These data allow us to  
138 characterize internal and superficial activity as well as to quantify, within the intrinsic methods’  
139 uncertainties, the size of the eruptions in terms of magma output rates and cumulative volumes based on

140 thermal satellite information. We also hypothesize some mechanisms to explain Sangay's long-term  
141 eruptive activity based on the extruded lava volume, the variations of the whole-rock geochemistry of the  
142 tephra products and the recorded geophysical parameters.

## 144 2. METHODS AND DATA PROCESSING

### 145 2.1. Ground-based monitoring network

146 Given the low risk associated with Sangay's activity and the extremely difficult access, the permanent  
147 monitoring network is modest. A single broadband seismometer (SAGA-BB) coupled with an acoustic  
148 sensor and a DOAS scanning instrument were installed 6 km from the summit in September 2013 (Fig. 1c).  
149 Nevertheless, extreme weather conditions and frequent ash fallout make it very difficult to keep these  
150 instruments working during long periods of time. As a result, the SAGA-BB has operated intermittently  
151 from September 2013 to the present, with no data during periods as long as a few months. Furthermore, the  
152 seismic digitizer had to be replaced in November 2018 due to complete damage. Consequently, most of the  
153 seismic activity at Sangay had to be complemented by nine regional broadband seismic stations located  
154 from 56 to 102 km away from the volcano (Fig. 1c). On the other hand, the DOAS scanning instrument  
155 provided good quality information only between December 2013 and June 2015 and again since December  
156 2019 when the spectrometer was replaced.

157  
158 In order to quantify the seismicity at Sangay, we calculated several parameters at SAGA-BB station and at  
159 the nine regional seismometers (Fig. 1c). For SAGA-BB, we first applied an STA/LTA (short-term average  
160 amplitude/long-term average amplitude) algorithm to count the number of transient events following the  
161 approach presented by Battaglia et al. (2016). We used a STA of 1 second and a LTA of 60 s, applied to  
162 data filtered between 0.5 and 20 Hz. Peak-to-peak amplitudes were calculated on-the-fly for each detection  
163 in the same frequency band. Secondly, to identify families of similar events, we extracted 20.48s signal  
164 windows for the vertical component of SAGA-BB, for all detections with an STA/LTA higher than 3.0. In  
165 total, we compared nearly 64,000 waveforms using cross-correlation, after filtering the waveforms between  
166 0.8 and 30 Hz. To build families we used open clustering allowing chain similarity (Battaglia et al. 2016)  
167 and a correlation threshold of 0.80.

168  
169 To complement and fill in observational gaps during SAGA outages, we also designed and implemented a  
170 subspace detector using the vertical component of the nine regional broadband seismometers (Fig. 1c).  
171 Subspace detectors are a class of correlation detectors but with the added benefit of being less sensitive to  
172 subtle changes in source-time history, mechanism, or location (Barrett and Beroza 2014; De La Hoz et al.  
173 2021). We employ the strategy of Harris (2006) to generate a design matrix of suitable events emanating  
174 from the volcano. For each regional sensor we filter, align, and build our basis functions (templates) from  
175 these matrices via singular value decomposition. Because of the large distances between this regional  
176 network and the volcano, and the generally low magnitude nature of the explosions, the signal is only  
177 coherent across a very narrow frequency range: we find that the signal to noise ratio is maximum in the 0.6  
178 – 1.2 Hz range. Our detector calculates a sufficient statistic (akin to a correlation coefficient) using an  
179 empirically-determined total of five basis functions. A detection is declared when the sufficient statistic  
180 surpasses a threshold of 0.1 on at least three channels. The selection of 5 basis functions and a detection  
181 threshold of 0.1 represents the best tradeoff between code execution time and rate of false positives. This  
182 procedure was run from August 2007 to May 2020 generating a total of ~238,000 detections.

183  
184 Unfortunately, because of the extremely narrow nature of the filter centered over 1 Hz, raw detections from  
185 the subspace detector are contaminated with numerous false detections from not only random noise but also  
186 local, regional, and even teleseismic earthquakes. To address this problem, we applied a binary  
187 classification algorithm written in MATLAB and using gentle adaptive boosting. This classifier was trained  
188 and validated on a suitably large dataset of true positives and known spurious detections (false positives).  
189 The training and validation sets were mutually exclusive to prevent data leakage, with respective labels  
190 being confirmed using the nearfield sensor SAGA-BB as ground truth. A total of 119 features for each  
191 event were extracted from the waveforms themselves and, consisted of various standard statistical measures  
192 such as mean, rms, kurtosis, amongst others. In the end, the most important features were the sufficient  
193 statistic itself, and the cross-correlation lag values (between sensors) of candidate events. After validation,  
194 we find that the classifier has a true positive identification rate of >97%, and false positive identification  
195 rate of >96%, which we find suitable for the purposes of this study since we seek only broad event detection  
196 capability for those periods of time when SAGA-BB is not transmitting. Finally, we apply the classifier to  
197 the entire dataset of ~238,000 detections, and we were able to prune this number down to ~98,000 total  
198 events detected between 2007 – 2020. This procedure constitutes a significant improvement in the  
199 homogeneity of the Sangay seismic catalog, albeit at the cost of a larger magnitude of completeness; in

200 general we find that the subspace detector coupled with the binary classifier can accurately identify the  
201 majority of Sangay events with amplitudes greater than  $\sim 8 \mu\text{m/s}$  as recorded on the SAGA instrument, with  
202 anything lower than  $8 \mu\text{m/s}$  being too low in amplitude to properly emerge from the noise ([Supplementary](#)  
203 [Material 1](#)).

204  
205 Finally,  $\text{SO}_2$  daily fluxes were calculated using the NOVAC software ([Johansson 2009](#)) introducing the  
206 wind conditions provided by NOAA wind models (National Oceanic and Atmospheric Administration,  
207 <https://www.ready.noaa.gov/READYamet.php>) calculated at the summit altitude of the volcano, assuming  
208 that the plume drifts horizontally at the vent altitude. Whenever Volcanic Ash Advisory Center (VAAC)  
209 alerts were available, we used the reported plume height, plume direction and velocity instead of the NOAA  
210 data. In addition, we calculated daily observed  $\text{SO}_2$  emission following the approach of [Hidalgo et al.](#)  
211 ([2015](#)). This approach is justified given that the dominant wind direction is towards the station.

## 212 213 **2.2. Satellite observations and overflights**

214 Satellite-based instruments are very useful tools for monitoring active volcanoes, in particular for those  
215 located in remote zones, as is the case of Sangay. We used the freely available data provided by the  
216 following systems: (1) Middle InfraRed Observation of Volcanic Activity (MIROVA,  
217 <https://www.mirovaweb.it/?action=volcanoes>) and Fire Information for Resource Management System  
218 (FIRMS, <https://firms.modaps.eosdis.nasa.gov>) that provided thermal information, (2) Washington VAAC  
219 alerts, which supplied information about the dispersal and height of ash plumes  
220 (<https://www.ssd.noaa.gov/VAAC/archive.html>), (3)  $\text{SO}_2$  mass derived from TROPOMI (TROPOspheric  
221 Monitoring Instrument) processed by Monitoring Unrest from Space (MOUNTS, <http://www.mounts->  
222 [project.com/home](http://www.mounts-project.com/home)), and from OMI sensor processed by National Aeronautics and Space Administration  
223 (NASA) via Global Sulfur Dioxide Monitoring (<https://so2.gsfc.nasa.gov/>), and (4) overflights to capture  
224 the volcanic products, in particular, lava flows and pyroclastic density currents, whenever the weather  
225 conditions allow to obtain clear images.

226  
227 We used an automated global hot spot detection system based on real-time Moderate resolution Imaging  
228 Spectroradiometer infrared data (MODIS), which then is processed by MIROVA ([Coppola et al. 2009,](#)  
229 [2013](#)). MIROVA completes automatic detection and location of thermal anomalies and provides a  
230 quantification of the Volcanic Radiative Power (VRP) in watts (W) ([Coppola et al. 2009, 2013, 2016, 2017](#)).  
231 From VRP we were able to derive Volcanic Radiative Energy (VRE), time-averaged discharge rate (TADR)  
232 and the cumulative lava volume according to the methodology proposed by several authors ([Coppola et al.](#)  
233 [2013, 2017; Naismith et al. 2019; Walter et al. 2019](#)). Volcanic Radiative Energy is the energy in Joules  
234 obtained by the trapezoidal integration of the Volcanic Radiative Power timeseries. Weekly time-averaged  
235 discharge rate is obtained from the average VRP during a period of seven days and the chemical  
236 composition of the extruded lavas. For this, we used the silica content of samples collected and analyzed  
237 in the 1990s ([Monzier et al. 1999](#)), and samples from this study corresponding to eruptive phases of 2015,  
238 2018, 2019 and 2020. Finally, the cumulative volume was estimated by using the weekly time-averaged  
239 discharge rate and a week time-integration, which we considered as the best approach at volcanoes that  
240 have strong cloud cover, as is the case of Sangay.

241  
242 Washington VAAC reports alerts for Sangay since January 2004. Since then, 900 confirmed alerts have  
243 been reported until 31 May 2020. Moreover, TROPOMI sensor ([Theys et al. 2019, Hedelt et al. 2019](#)) on  
244 board Sentinel-5P provides  $\text{SO}_2$  vertical column densities maps since 2018. The volcano monitoring system  
245 MOUNTS ([Valade et al. 2019](#)) converts these into daily  $\text{SO}_2$  masses, with a spatial filter allowing its  
246 attribution to Sangay. Finally, sporadic overflights (one or two per year) using a visual and a FLIR thermal  
247 camera complemented with satellite images (Suomi-NPP, Aqua and Terra) provided by the Fire  
248 Information for Resource Management System, give information on the emplacement of lavas and  
249 pyroclastic density current deposits. In order to filter out wrong satellite location of the thermal anomalies  
250 because of the angle between the satellite flight and the topography, we applied a  $<0.5$  threshold on the  
251 satellite-track data ([Wang et al. 2017](#)).

## 252 253 **2.3. Volcanic products geochemistry**

254 We analyzed bulk ash samples from the 2015, 2018, 2019 and 2020 eruptions collected at SAGA-BB site  
255 ([Fig. 1c](#)). Major and trace elements were determined at the PSO/IUEM (Pôle Spectrométrie Océan, Institut  
256 Universitaire Européen de la Mer, Brest, France), following the analytical procedure of [Cotten et al. \(1995\)](#).  
257 Typically, 250 mg of rock powder were dissolved in closed screw-top teflon vessels (Savillex) at about  $90^\circ\text{C}$   
258 for one day using 3 ml of concentrated HF, and 1 ml of concentrated  $\text{HNO}_3$ . Next, 96 ml of  $\text{H}_3\text{BO}_3$  aqueous  
259 solution (20 g/L  $\text{H}_3\text{BO}_3$ ) were added to neutralize the excess HF. All reagents used are analytical grade.

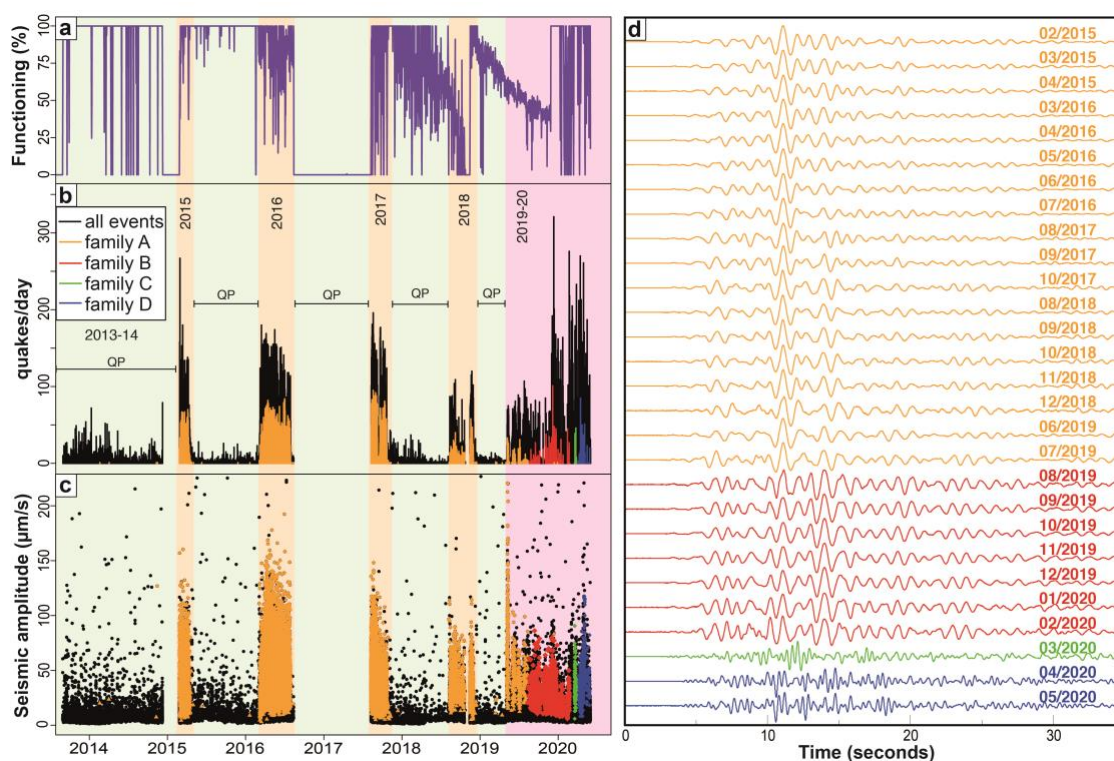
260 Elements were measured by inductively coupled plasma-atomic emission spectrometry (ICP-AES) using a  
 261 Horiba Jobin Yvon® Ultima 2 spectrometer. The boron included in the solution was used as an internal  
 262 standard. Calibrations were made using international standard, ACE, WSE, JB2. For major elements,  
 263 relative standard deviation is  $\leq 1\%$  for  $\text{SiO}_2$  and  $\leq 2\%$  for the other major elements. Finally, we used for  
 264 comparison the geochemical data of most recent products (1990s) from Sangay's summit area reported by  
 265 Monzier et al. (1999) (Supplementary Material 2).  
 266

### 267 3. RESULTS

#### 268 3.1. Seismic activity

##### 269 3.1.1. Local seismic observations

270 Despite the intermittence of SAGA-BB (Fig. 2a), we were able to identify quiescent and eruptive phases  
 271 based on the number and amplitude of the seismic events recorded from September 2013 to May 2020 (Fig.  
 272 2b & 2c). Quiescent phases are characterized by a low number of detections, mostly related to background  
 273 noise or regional events (Fig. 2b). In contrast, eruptive phases display clear peaks above background level  
 274 in both number of events and amplitude, reaching more than 100 seismic events per day and amplitudes  
 275 above  $60 \mu\text{m/s}$  (Fig. 2b & 2c). In addition, we observed that there is no evident escalating unrest before  
 276 eruption onsets (Fig. 2b).  
 277



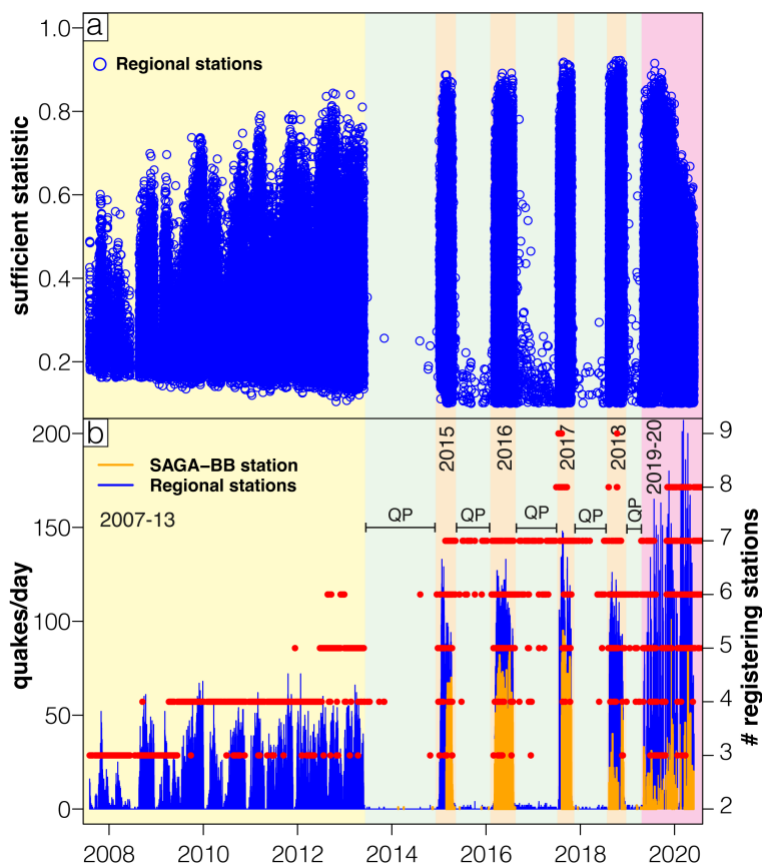
278  
 279 **Fig. 2** a) Functioning of SAGA-BB in percentage of time per day, b) Number of seismic events per day, black bars  
 280 represent all detected events, while orange, red, green, and blue bars display the number of events belonging to each  
 281 seismic family, c) amplitude of the events also separated by family and expressed in  $\mu\text{m/s}$ . Green background shows  
 282 quiescent phases (QP) while orange and red backgrounds correspond to eruptive phases. d) Similar waveforms showing  
 283 monthly stacks for the main families. Each waveform corresponds to a stack of all similar events identified during a  
 284 given date listed at the end of each line. The waveforms were detected during all periods of observation.  
 285

286 We identified four major seismic families on SAGA-BB which occurred successively and only during  
 287 eruptive periods (Fig. 2b & 2c). They are active only one at a time. The transition between families A and  
 288 B (August 2019) is likely caused by a change in the instrument response as the station was suddenly tilted  
 289 and flooded at the time of the transition. On the other hand, the two later transitions (March and April 2020)  
 290 may be related to changes in the source or morphology of the volcano (Fig. 2d). Regional stations are too  
 291 distant to record the finer details in the waveforms that SAGA-BB provides, though some broad degradation  
 292 in waveforms similarity is discernable and match to a degree the observations seen at SAGA-BB, in  
 293 particular the March 2020 transition (Fig. 3a).  
 294

295 Overall, many of the events belonging to these families display acoustic waveforms on the infrasound  
 296 channel, indicating that they are explosion quakes. Figure 2d displays monthly stacked waveforms showing  
 297 a great similarity over years but also a significant change in the waveform and frequency content since  
 298 March 2020. These events can be interpreted as the resonance of the conduit and surrounding volcanic  
 299 edifice in response to the explosive decompression of the magma (Battaglia et al. 2016). Details of these  
 300 modes of oscillation are filtered by the distance, inducing the presence of a single family during most of  
 301 the study period. Some of the explosion quakes are also followed by long oscillations, sometimes  
 302 monochromatic, possibly corresponding to chugging following the initial explosions whose waveforms are  
 303 identical to shorter events, similar to what is described by Johnson and Lees (2000). The families group  
 304 between 0 and 90% of the daily larger events ( $STA/LTA > 6$ ) during eruptive periods with a global average  
 305 at  $40 \pm 24\%$ . This indicates the presence of a significant and dominating stable explosive process during  
 306 these phases. A general tendency to decrease toward the end of the study period is observed. Further  
 307 investigation is needed to better understand the changes that occurred in March 2020.  
 308

### 3.1.2. Regional seismic network

310 Near-field seismic monitoring of Sangay volcano has proven difficult to keep running continuously due to  
 311 its remote location and frequent cloud and ash coverage, although efforts are currently underway to expand  
 312 the network and improve the reliability of existing instrumentation. In the meantime, the subspace detector  
 313 described above has been refined enough that it provides a suitable, albeit lower resolution, alternative to  
 314 seismic monitoring for those periods when SAGA-BB is not available (Fig. 3b). This subspace detector  
 315 cannot distinguish between explosions or regular LPs, cannot track changes in waveforms to nearly the  
 316 same degree as a local network, and the magnitude threshold is relatively high, where in general any signal  
 317 less than  $8 \mu\text{m/s}$  (as recorded at SAGA-BB) would not be detectable at regional distances. However, the  
 318 primary advantage of the regional network is its more uniform homogeneity in time, which is important for  
 319 not only operational monitoring in near real time but also for retrospective studies such as this one where  
 320 the regional stations allowed to expand the seismic record of Sangay backwards in time, allowing to  
 321 quantify the number of discrete seismic events since August 2007 (Fig. 3b). Interestingly, on a daily basis,  
 322 regional detections could be higher than the quake counting in SAGA-BB. This is mainly due to the  
 323 incomplete recordings from SAGA-BB (Fig. 2a).  
 324



325 **Fig. 3** a) Values of sufficient statistic of the subspace detector as a function of time, which can be considered a proxy  
 326 for waveform coherence relative to the original set of 5 basis functions across the 9 regional sensors. A subtle drop in  
 327



the value of the sufficient statistic is seen towards the end of 2019 and into 2020, coincident with results obtained from the SAGA analysis, b) comparison between the number of seismic events from Sangay as detected at SAGA-BB (orange) and the nine regional seismic stations (blue). Red dots are the number of regional stations used to detect each discrete event. Green background shows quiescent phases (QP) while yellow, light orange and red backgrounds correspond to eruptive phases.

Table 1 summarizes the seismic activity at Sangay between August 2007 and May 2020 based on the regional network. Three main eruptive periods were identified. During the period from 4 August 2007 to 29 May 2013 the activity at Sangay was long-lasting and fluctuating. Average transient events reached  $18 \pm 17$  events/d with a maximum of 72 and a median of 15 events/d. In contrast, between 2015 and 2018, four clear short episodic eruptions occurred one each year, as previously identified on SAGA-BB (Fig. 2b). During this period, the four phases were statistically similar. They lasted  $\sim 100$  days each and their transient events significantly increased in comparison with the previous period reaching  $\sim 81 \pm 30$  per day with a median of 86 and a maximum of 148 events/d. In addition, the 2019-2020 period showed fluctuating and long-lasting activity similar to what was observed during the first period between 2007 and 2013, but the daily event rate is three times higher. Average transient events reached  $52 \pm 50$  events/day with a median of 40 and a maximum of 207 events/d, which corresponds to the maximum registered during the entire study period. Finally, the five repose periods recognized in between the eruptive phases display a minimum seismic activity with an average lower than one seismic event per day (Fig. 3). This agrees with the no escalating unrest before eruptions observed at SAGA-BB (Fig. 2b).

**Table 1.** Statistical summary of the seismic and gas emission data based on 9 broadband regional seismic stations and the SAGA-DOAS station. Additionally, time-averaged discharge rate (TADR) and cumulative volume extruded at Sangay volcano are shown. \*values are estimated from 2001. QP = Quiescent Phase, VM = valid measurements, DVMD = daily validated measurement duration.

Eruptive Phase	2007-2013	QP 1	2015	QP 2	2016	QP 3	2017	QP 4	2018	QP 5	2019-2020
Onset	04.08.07	30.05.13	04.01.15	19.04.15	08.03.16	31.07.16	20.07.17	28.07.17	11.08.18	09.12.18	06.05.19
End	29.05.13	03.01.15	18.04.15	07.03.16	30.07.16	19.07.17	27.10.17	10.08.18	08.12.18	05.05.19	31.05.20
Duration (d)	2125	584	105	324	145	354	100	287	120	148	392
Average seism/d	$18 \pm 17$	$0.1 \pm 0.3$	$72 \pm 30$	$0.3 \pm 0.8$	$88 \pm 25$	$0.5 \pm 0.9$	$83 \pm 39$	$0.1 \pm 0.4$	$80 \pm 28$	$0.6 \pm 1$	$52 \pm 50$
Median seism/d	15	0	77	0	95	0	93	0	86	0	40
Max. seism/d	72	5	133	6	133	5	148	3	126	7	207
Cum. Seism	38781	31	7568	100	12767	187	8330	40	9595	86	20339
#VM SO <sub>2</sub>	-	1-4	1-6	1-9	-	-	-	-	-	-	1-28
DVMD (min)	-	11-72	18-108	10-162	-	-	-	-	-	-	13-414
SO <sub>2</sub> flux (t/d)	-	$11 \pm 26$	$10 \pm 32$	$39 \pm 53$	-	-	-	-	-	-	$229 \pm 277$
Max SO <sub>2</sub> flux (t/d)	-	219	224	242	-	-	-	-	-	-	2435
TADR (m <sup>3</sup> /s)	$0.28 \pm 0.29^*$	-	$0.8 \pm 0.56$	-	$1.3 \pm 1.16$	-	$1.35 \pm 1.08$	-	$1.47 \pm 0.63$	-	$5 \pm 4.1$
TADR max (m <sup>3</sup> /s)	2.07*	-	2.95	-	5.65	-	5.16	-	3.55	-	21.8
Cum. Volume (Mm <sup>3</sup> )	$100 \pm 50^*$	-	$6.8 \pm 3.4$	-	$15.8 \pm 7.9$	-	$15.8 \pm 7.9$	-	$15.1 \pm 7.6$	-	$172 \pm 85.8$

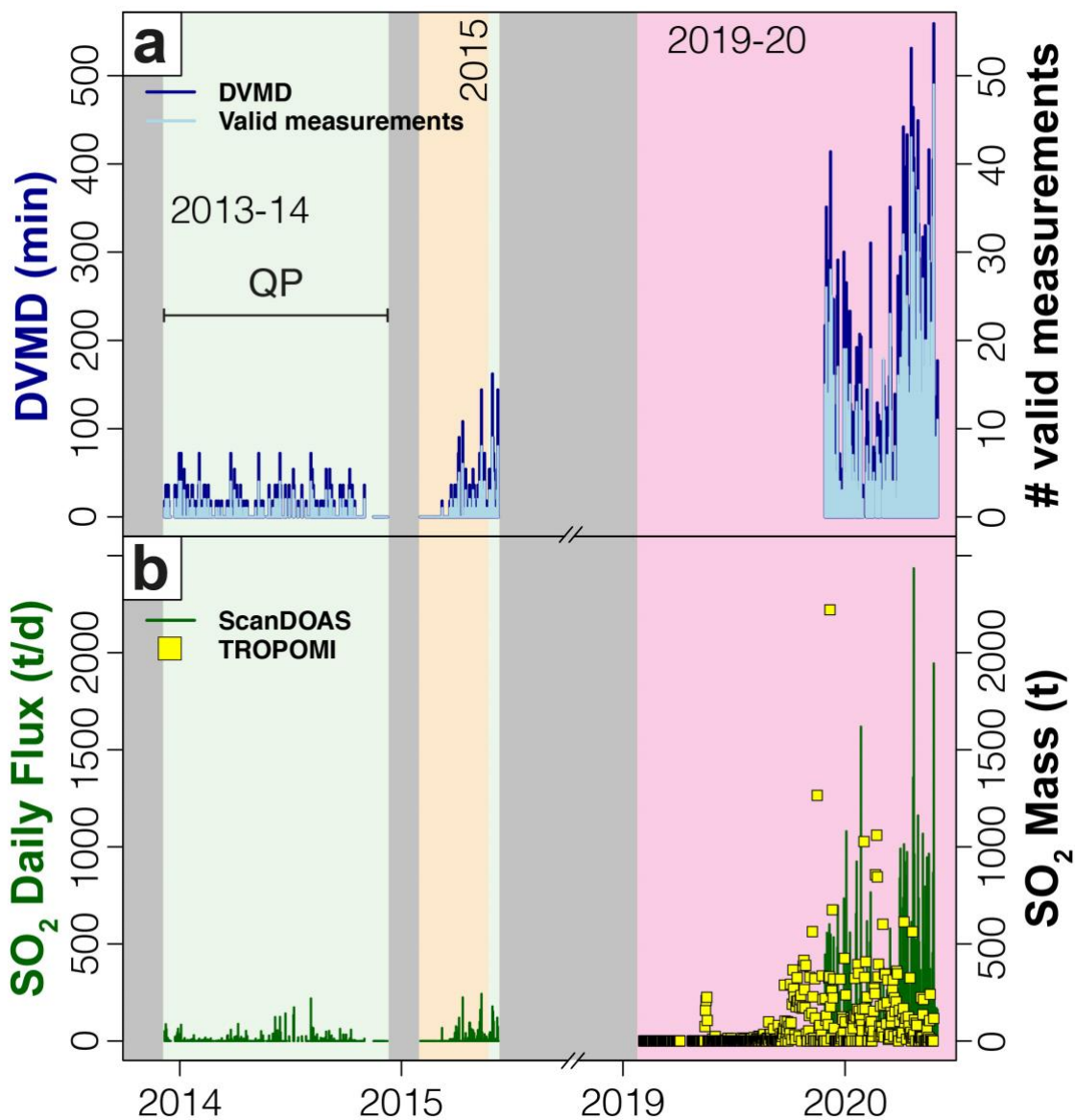
Interestingly, the daily seismic event counting reconstructed for Sangay fits nicely with the satellite-based observations, especially with the thermal and VAAC alerts, validating and providing complementary data to understand eruptive dynamics (see section 3.3). This confirms the overall long-lasting activity since at least 2007 until 2013, the episodic activity from 2015 to 2018, and the increased eruptive activity starting in 2019 and still ongoing until the time of writing of this manuscript (March 2022).

### 3.2. SO<sub>2</sub> emissions

The ScanDOAS instrument worked intermittently. Nevertheless, it could record data from: the quiescent phase of 2013-2015 (52%), the 2015 eruption (72%), part of the quiescent phase between 2015 and 2016 (16%) and the ongoing eruption from November 2019 to May 2020 (23%). Percentages refer to the functioning days of the station in respect to the duration of the quiescence or eruptive phase.

During the first quiescence phase (2013-2015), SAGA-DOAS detected between 1 and 4 valid measurements for 11-72 minutes of daily valid measurement duration (DVMD), which corresponds to the measuring time (in minutes) of all valid scans throughout a day (Fig. 4a, Table 1). The observed SO<sub>2</sub> flux ranged from 2 to 219 t/d with an average of  $11 \pm 26$  t/d (Table 1). During the 2015 eruptive period the station registered a slight increase in the number of valid measurements (1-6) and DVMD (18-108 minutes, Fig. 4a). However, the SO<sub>2</sub> flux was  $10 \pm 32$  t/d average with a maximum single measurement of 224 t/d, like

372 the previous quiescence phase (Fig. 4b). In the second quiescence period (2015-2016): 1 to 9 valid  
 373 measurements were detected with 10-162 minutes of DVMD. The SO<sub>2</sub> flux reached 39±53 t/d, with a  
 374 maximum single measurement of 242 t/d (Table 1). Finally, the current eruption shows a significant  
 375 increase in all the parameters. The daily valid measurement duration lies between 13-414 min with 1-28  
 376 valid measurements per day. The SO<sub>2</sub> flux ranges from 12 to 2435 t/d with an average of 229±277 t/d (Table  
 377 1). In summary, we identified an increase in DVMD and the number of valid measurements between  
 378 quiescent and eruptive phases (Fig. 4a). Interestingly, the SO<sub>2</sub> fluxes lay in the same order of magnitude  
 379 during the 2013-2015 period, which corresponds to two quiescence (QP1 & QP2) and the 2015 eruptive  
 380 phase (Table 1). In contrast, the 2019-2020 eruptive period displays a significant increase in SO<sub>2</sub> measured  
 381 degassing as well as daily valid measurement duration (Fig. 4b, Table 1).  
 382



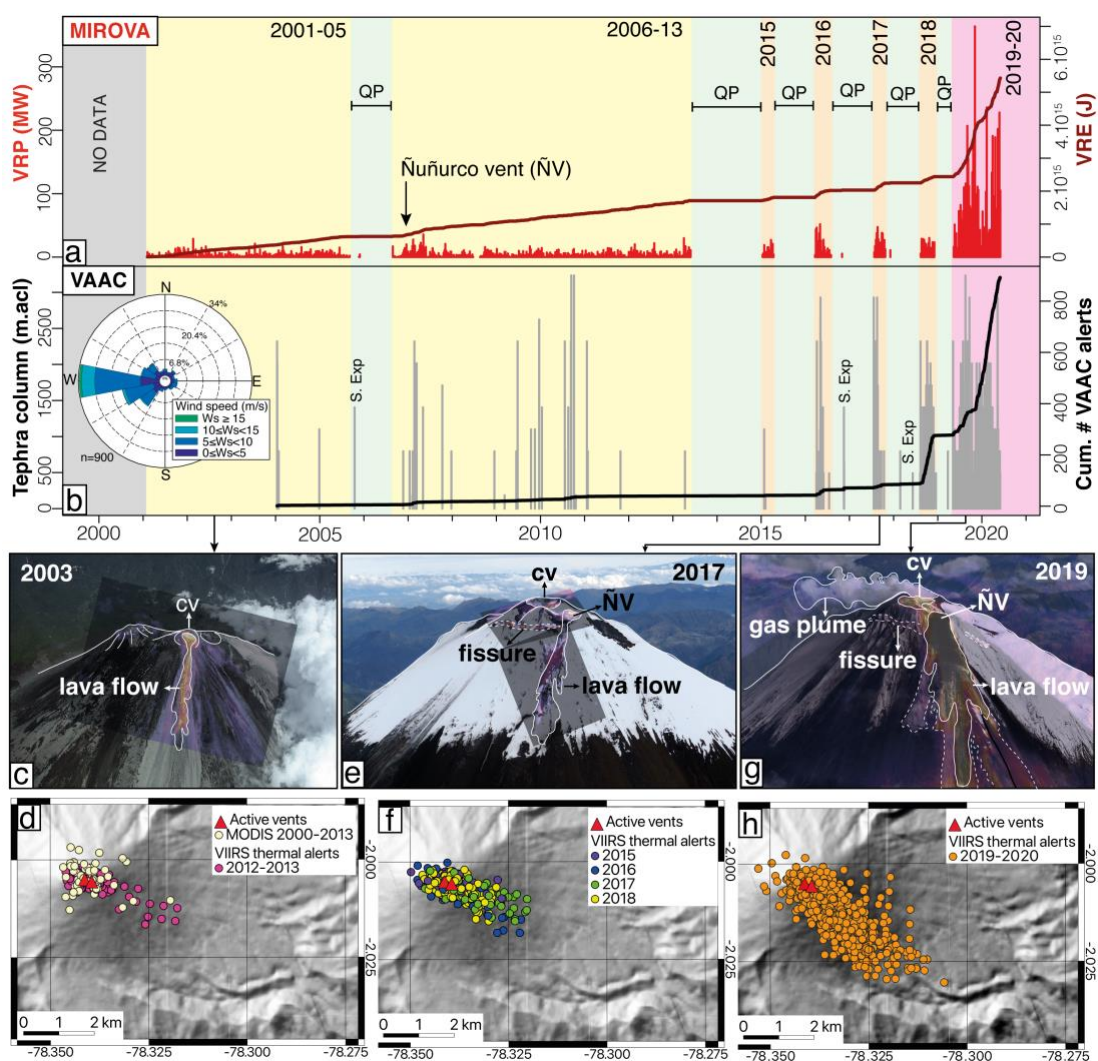
383 **Fig. 4** SO<sub>2</sub> data from the ScanDOAS station located at 6 km downwind from Sangay crater. a) Dark and light blue bars  
 384 show the daily validated measurement duration (DVMD) and number of valid measurements respectively, b)  
 385 comparison between daily SO<sub>2</sub> fluxes (DOAS sensor) from December 2013 to May 2020 and the SO<sub>2</sub> mass derived  
 386 from (MOUNTS, TROPOMI sensor). Note that SO<sub>2</sub> is expressed in t/d and masses derived from TROPOMI in tons.  
 387 Gray backgrounds are periods without data from the DOAS instrument, green background shows quiescent phases  
 388 (QP) while orange and red backgrounds represent eruptive phases.  
 389

390  
 391 The satellite OMI sensor indicates negligible SO<sub>2</sub> between 2004 and August 2019, while from September  
 392 2019 to May 2020, it reported sporadic SO<sub>2</sub> emissions ranging from 30 to 1000 tons at Sangay.  
 393 Additionally, TROPOMI data processed by MOUNTS identified daily SO<sub>2</sub> degassing since the onset of the

394 eruption in May 2019, with an average of 170 tons and a maximum of 2221 tons on 12 December 2019  
 395 (Fig. 4b).  
 396

### 397 3.3. Thermal power and ash plume height

398 Figure 5 summarizes the observations of the subaerial activity of Sangay volcano between January 2001  
 399 and May 2020 recorded by various satellite instruments. Both thermal and ash emission alerts clearly show  
 400 eruptive phases and quiescence over time (Fig. 5a & 5b). From 2001 to 2013, the eruptive activity was  
 401 sparse, but long-lasting and the weekly Volcanic Radiative Power was lower than 60 MW (the maximum  
 402 registered in this period). The activity paused between 2005 and 2006. After this activity interruption, in  
 403 2007, the Ñuñurcu vent appeared 210 m southeast of the Central Crater increasing the slope of the Volcanic  
 404 Radiative Energy (Fig. 5a). Eruptive activity paused again in 2013 for a period of 21 months. Between 2015  
 405 and 2018, episodic eruptions occurred at the rate of 1/year, all of them separated by well-defined quiescent  
 406 phases (Fig. 5a & 5b). During those eruptions, weekly volcanic radiative power was still lower than 60 MW  
 407 (Fig. 5a). In contrast, the 2019-ongoing activity marked a significant increase in eruption intensity, reaching  
 408 the highest weekly volcanic radiative power, up to 300 MW, with several minor peaks. The volcanic  
 409 radiative energy curve also shows a significant increase in slope during this eruptive period (Fig. 5a).  
 410



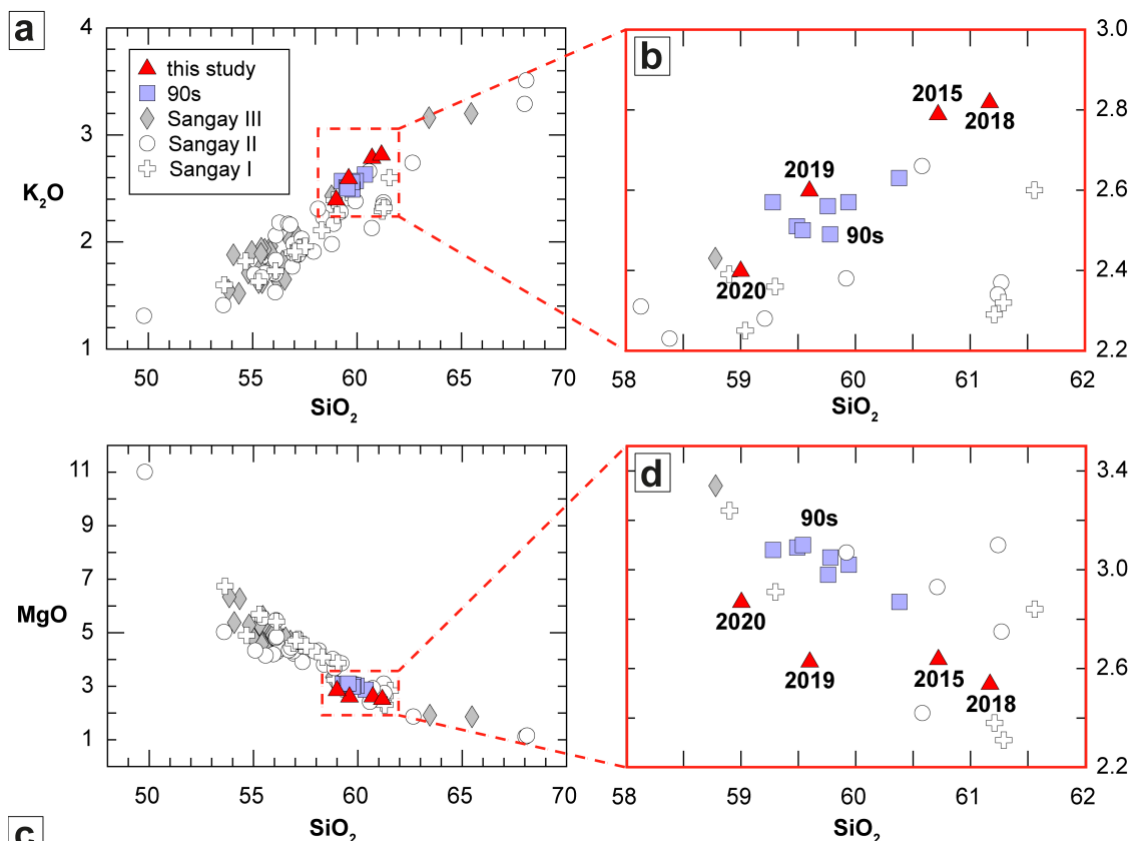
411 Fig. 5 a) Composite graph of the thermal anomalies recorded by MIROVA. On the left axis is the Volcanic Radiative  
 412 Power (VRP) in megawatts and on the right axis weekly Volcanic Radiative Energy (VRE) in Joules. b) Washington  
 413 VAAC confirmed alerts from January 2004 to May 2020 in meters above the crater level (m.acl), cumulative number  
 414 of alerts is shown on the right axis. Wind rose diagram displaying predominant wind direction and speed obtained from  
 415 VAAC. Single explosions in between periods are shown as "S. Exp". Colored backgrounds separate the eruptive from  
 416 quiescent phases (QP). Data downloaded from <http://www.mirovaweb.it/>  
 417 and <https://www.ssd.noaa.gov/VAAC/messages.html>  
 418 respectively. From c) to h) composition of photographs and thermal images illustrating the active vents and products over the study period and maps displaying the locations of MODIS  
 419 and VIIRS thermal anomalies centers from the different eruptive phases based on FIRMS  
 420 <https://firms.modaps.eosdis.nasa.gov/map/>.  
 421

422 Figure 5b displays volcanic ash cloud occurrence according to Washington VAAC alerts. Plume heights  
 423 are less than 3.5 km above the crater level, being similar throughout the entire period. Single isolated  
 424 explosions in between eruptive phases also occurred. Throughout the study period, most of the ash clouds  
 425 showed a westward drift (Fig. 5b), which agrees with the predominant wind direction in the Ecuadorian  
 426 Andes. Finally, the cumulative number of ash alerts shows a significant increase during the 2018 and 2019-  
 427 ongoing eruptive phases (Fig. 5b).

429 Between 2001 and 2005 the activity was characterized by explosions and lava flows extruded from the  
 430 Central Crater (Fig. 5c). Nonetheless, since 2007, ash emissions were focused on the central crater and the  
 431 lava flows were emitted from the new Ñuñurcu vent (Fig. 5e & 5g). Pyroclastic density currents related to  
 432 lava front collapses also occurred throughout the entire study period, usually reaching a run-out distance of  
 433 < 3 km towards the eastern and southeastern flanks (Fig. 5d & 5f). However, during 2019-ongoing eruption,  
 434 pyroclastic density currents reached more than 4 km from the vent, with a maximum length of 7.6 km on  
 435 11 December 2019 (Fig. 5h), which is significantly larger than those observed in any previous eruptive  
 436 phase (Fig. 5d & 5f). As a result, the occurrence of secondary lahars triggered by heavy rainfall that  
 437 remobilizes this loose material has become a typical phenomenon during the ongoing eruption and has  
 438 temporarily dammed the Upano river at its confluence with the Río Volcán, 25 km away from the summit  
 439 (Fig. 1c).

### 441 3.4. Ash composition

442 Whole-rock analyses of bulk ash show a slight shift in silica content through time. This is plotted on the  
 443 classification diagram of Peccerillo and Taylor (1976) in figure 6. Sangay's products are low-K basalts and  
 444 andesites. Bulk tephra samples from 2015 to 2018 show similar ~61wt% SiO<sub>2</sub> content, while 2019 and  
 445 2020 ashes are slightly more basic (59.6 - 59.0wt% SiO<sub>2</sub>), closer to the 1990s magma compositions taken  
 446 from Monzier et al. (1999) (Fig. 6a & 6b). MgO compositions also show an increasing trend confirming  
 447 the similarity of the most recent products to the samples erupted during the 1990s (Fig. 6c & 6d).

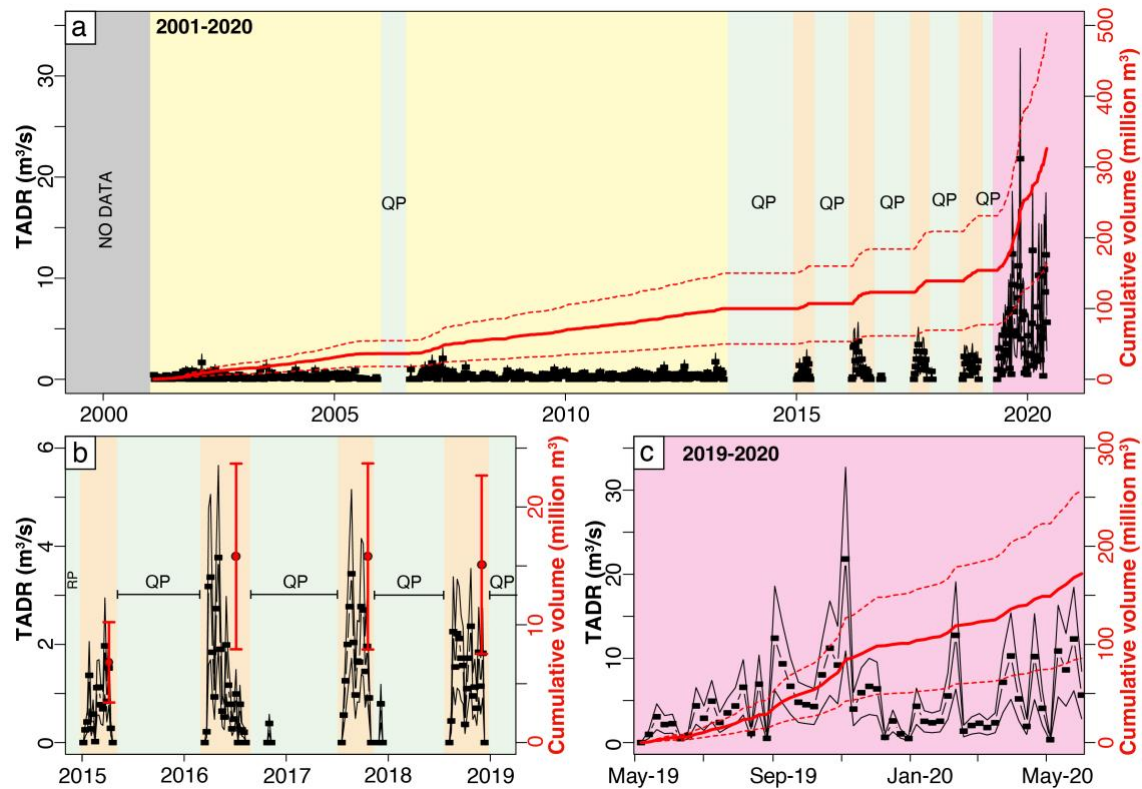


449 **Fig. 6** a) K<sub>2</sub>O vs. SiO<sub>2</sub> diagram for Sangay's bulk ash compositions for 2015, 2018, 2019 and 2020 samples compared  
 450 to previous geochemical data from Monzier et al. (1999). b) Zoom on K<sub>2</sub>O vs. SiO<sub>2</sub> diagram showing the recent  
 451 products compositions. c) MgO vs. SiO<sub>2</sub> diagram, and d) Zoom on the MgO vs. SiO<sub>2</sub> diagram. Error in analyses is  
 452 smaller than the size of the symbols.  
 453  
 454  
 455

456  
457  
458  
459  
460  
461  
462  
463  
464  
465  
466  
467  
468  
469  
470  
471  
472  
473  
474  
475  
476

### 3.5. Time-Averaged Discharge Rate (TADR) and cumulative volume estimation

The volumes of erupted lava and the TADRs were calculated by means of the thermal data acquired by satellite. The thermal approach is based on the empirical relationship between radiant energy (VRE) and erupted lava volumes (Vol) which can be expressed through a best-fit coefficient so that  $VRE/Vol = \text{crad}$  (radiant density) (Coppola et al. 2013). It has been shown that this coefficient varies from volcano to volcano and is strongly influenced by the rheology of the erupted lava, the latter represented roughly by the silica content (Coppola et al. 2013). We calculated the radiant density (crad) for Sangay using the silica content from the ash sampled at the SAGA-BB site and from literature data (Fig. 6). For the eruptive period between 2001 and 2013 we used the average 59.44wt% SiO<sub>2</sub> for the 1990s eruptive products reported in Monzier et al. (1999). For the 2015, 2016 & 2017 eruptions we used 60.72wt% SiO<sub>2</sub>, which is the silica content of 2015 ashes, for the 2018 eruption 61.17wt% SiO<sub>2</sub>, and for 2019 and 2020 we used 59.6 and 59.0 wt% SiO<sub>2</sub>, respectively. The derived radiant densities are:  $2.29 \times 10^7$  (2001-2013),  $1.83 \times 10^7$  (2015-2017),  $1.70 \times 10^7$  (2018),  $2.22 \times 10^7$  (2019) and  $2.47 \times 10^7$  (2020)  $\pm 50\%$  J/m<sup>3</sup>. Afterwards, we calculated minimum, mean and maximum time-average discharge rate and cumulative volume including uncertainties. It should be noted that the approach is valid under the fundamental assumption that radiant heat detected by MODIS is exclusively sourced from “effusive/extrusive activity” (Coppola et al. 2013). However, if additional heat sources are produced by other volcanic phenomena/products (i.e. explosions, collapses of lava flow front, pyroclastic density currents) the volumes obtained with the thermal proxy are probably overestimated. Since at Sangay volcano we are unable to quantify the proportion of heat sourced by “non-effusive activity” our estimate should be taken with caution and considered as maximum values.



477  
478  
479  
480  
481  
482  
483  
484  
485  
486  
487  
488  
489  
490  
491

**Fig. 7** TADR (black lines) and cumulative volume (red lines) for Sangay volcano derived from MIROVA thermal data and the methodology proposed by (Coppola et al. 2009, 2013, 2017). Colored backgrounds represent the eruptive stages and quiescence phases (QP) from a) January 2001 to May 2020, b) between 2015 and 2018, c) during 2019-2020 ongoing eruptive period. Note that black squares are the mean TADR and black and dashed red lines depict the error of the TADR and volume estimations, respectively.

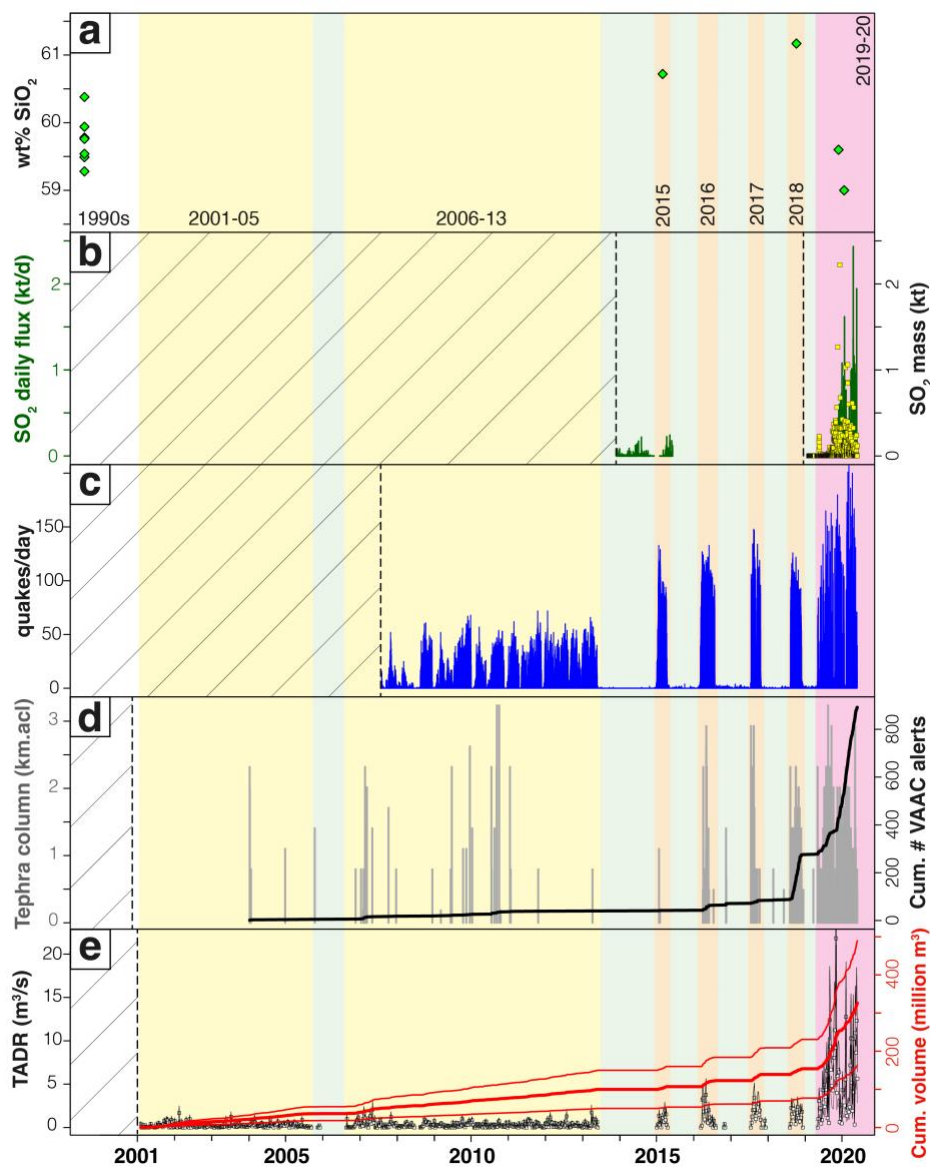
Figure 7a displays the estimated time-average discharge rate (TADR) and cumulative magma volume emitted throughout the last two decades. From 2001 to 2020, Sangay volcano extruded between 0.02 and 21.8 m<sup>3</sup>/s (TADR), which implies a cumulative extruded lava volume of  $326 \pm 163$  million m<sup>3</sup>. A third of the volume was emitted during the long-lasting period of 2001-2013, reaching  $100 \pm 50$  million m<sup>3</sup> with a time-average discharge rate of  $0.28 \pm 0.29$  m<sup>3</sup>/s and a maximum of 2.07 m<sup>3</sup>/s (Table 1). During the episodic period a cumulative volume of  $53.5 \pm 26.8$  million m<sup>3</sup> was extruded with the mean TADR ranging from 0.02 to 3.77 m<sup>3</sup>/s. The 2015 eruption extruded  $6.8 \pm 3.4$  million m<sup>3</sup>, while the 2016, 2017 and 2018 eruptive phases emitted similar volumes of  $15.8 \pm 7.9$  million m<sup>3</sup>,  $15.8 \pm 7.9$  million m<sup>3</sup> and  $15.1 \pm 7.6$  million m<sup>3</sup>,

492 respectively (Fig. 7b, Table 1). Finally, the 2019-2020 period shows a significant increase in both time-  
 493 average discharge rate reaching  $5 \pm 4.1 \text{ m}^3/\text{s}$  with a maximum of  $21.8 \text{ m}^3/\text{s}$  and a cumulative volume of  
 494  $172 \pm 85.8$  million  $\text{m}^3$  of lava (Fig. 7c, Table 1), making this last period the largest and most energetic during  
 495 the past 20 years (Fig. 7a). Time-average discharge rate during the last period is five times higher than the  
 496 previous ones. This significant increase could explain the high recurrence of lava front collapses and  
 497 associated co-pyroclastic plumes (Fig. 5b), in addition to the intense erosion of Volcán ravine observed at  
 498 the southeastern flank. Finally, the cumulative volume indicates that Sangay volcano has become more  
 499 active over time, which implies a sustained increase of the global average discharge rate (Fig. 7a).  
 500

#### 501 4. DISCUSSION

##### 502 4.1. Interpretations of eruptive activity based on clustering of multiparametric monitoring data

503 Based on the simple temporal clustering of the seismic catalog, thermal and ash emission alerts (Figs. 3b,  
 504 5a & 5b), we identified well-defined quiescence episodes between seven eruptive phases from 2001 to 2020  
 505 (Fig. 8). We grouped these various phases into three main eruptive periods: mild long-lived activity from  
 506 2001 to 2013, episodic eruptions between 2015 and 2018, and continuous and very intense activity since  
 507 2019 (yellow, orange, and red backgrounds, respectively in Fig. 8).  
 508



509 **Fig. 8** Composite temporal series from 1990s to 2020. a) wt% SiO<sub>2</sub> whole rock analysis of the eruptive products, b)  
 510 daily SO<sub>2</sub> flux (SAGA-DOAS) and mass (MOUNTS), c) quakes per day based on the regional seismic network, d)  
 511 eruptive column height in km acl and cumulative Washington VAAC alerts, e) Time Average Discharge Rate (TADR)  
 512 and cumulative volume of the extruded lavas based on VRP provided by MIROVA system. Colored backgrounds  
 513 represent the eruptive (yellow, orange and red) and quiescence (green) phases. Dashed lines depict the onset of the  
 514 different monitoring systems at Sangay.  
 515

516 SiO<sub>2</sub> compositions of Sangay's products in the 1990s ranged from 59.28 to 60.38 wt% (Monzier et al.  
517 1999). In 2015 and 2018 ash compositions were slightly more acidic (60.7 - 61.1 wt%, respectively), while  
518 the current activity expelled ashes with lower SiO<sub>2</sub> contents (59.6 and 59.0 wt% SiO<sub>2</sub>, Fig. 8a), similar to  
519 that of the 1990s. Overall, it seems that long-lasting activity matches with the less evolved magmas, while  
520 episodic activity takes place whenever compositions are slightly more acidic. The lower SiO<sub>2</sub> content of the  
521 ongoing eruptive products coupled to a higher MgO content (2.63-2.87 wt% in Fig. 6d) indicates an  
522 injection of a more basic magma into the system. Given the few data and the quality of the ash samples,  
523 future work should focus on robust sampling of fresh lava to improve the geochemical patterns presented  
524 here and to better understand Sangay's magmatic system including magma reservoir(s) location,  
525 crystallization and magma replenishment processes. However, despite the low number of samples, the  
526 observed changes in SiO<sub>2</sub> lie beyond the analytical error, indicating that they are meaningful.

527  
528 SO<sub>2</sub> degassing at Sangay started to be monitored at the end of 2013 (Fig. 8b green bars). For the period  
529 2013-2015 daily SO<sub>2</sub> fluxes are in the same order of magnitude (~10<sup>2</sup> t/d) throughout both, quiescence and  
530 episodic eruptive phases. We interpret this as reflecting either, or a combination of: (1) crystallization-  
531 induced volatile saturation (Tait et al. 1989) of the remaining non-eruptible 2001-2013 magma, promoting  
532 its evolution towards more acidic compositions and its eruption by second boiling (Putirka 2017); (2) small  
533 magma injections, which only provided gas and heat that reactivated the shallow reservoir without reaching  
534 the surface (Humphreys et al. 2007). These two mechanisms (individually or combined) would cyclically  
535 have taken place triggering the four short-lived phases observed between 2015 and 2018, as well as the  
536 shift to slightly more acidic compositions, accompanied by similar SO<sub>2</sub> emissions during quiescence and  
537 eruptive phases. Unfortunately, the station stopped working from 2015 to 2019, so there is not enough data  
538 to confirm if degassing levels stayed similar during quiescence and eruptive phases and to assess which  
539 mechanism(s) controlled the episodic eruptive activity during this period. Therefore, the observed episodic  
540 activity could also be explained by (3) cycles of crystallization-driven plug formation which lead to  
541 progressive gas accumulation triggering the episodic eruptions once the gas pressure overcame the  
542 resistance of the plug (Battaglia et al. 2019; Woitischek et al. 2020). Finally, for the 2019-ongoing eruption,  
543 both ground-based and satellite SO<sub>2</sub> monitoring systems registered a significant increase in SO<sub>2</sub> emissions  
544 (Fig. 8b). This could be interpreted as the refill of the shallow reservoir by a more basic and gas-rich magma  
545 that ascended from depth (Putirka 2017).

546  
547 The regional seismic network allowed to identify low, oscillating, and long-lasting activity from 2007 to  
548 2013 (Fig 8c). This fluctuating behavior could be related to gas waves that promoted episodes of more  
549 intense activity alternated with repose intervals over periods of days as proposed by Michaut et al. (2013).  
550 On the contrary, between 2015 and 2018 intense but short-lived eruptions occurred, as can be observed in  
551 the increased number of explosion quakes per day (Fig 8c). This activity could have been triggered by  
552 degassing-induced second boiling during its respective preceding quiescence periods, as the SO<sub>2</sub> data  
553 suggests. In 2019-2020 we observed an oscillating but increased number of quakes per day compared to  
554 the entire 2007-2018 period (Fig 8c). This could be related to a magma intrusion that ascended from depth,  
555 supporting the hypothesis presented previously based on the geochemical and SO<sub>2</sub> data (Fig 8a & 8b).  
556 Additionally, the occurrence of a single seismic family (A) from January 2015 to March 2020 suggests that  
557 there is only one dominating eruptive process (explosion type) throughout all active periods (Fig. 2). After  
558 March 2020, two more seismic families appeared (C, D in Fig. 2), possibly indicating the involvement of  
559 new eruptive processes and/or significant changes in Sangay's morphology.

560  
561 Eruptive plumes at Sangay are emitted via minor explosive activity and ash venting from the Central Crater.  
562 The average height of the plumes has been of 1±0.6 km acl (Fig. 8d), corresponding to 6.3±0.6 km asl  
563 throughout the entire study period. Even though in 2019-2020 eruptive activity increased in various  
564 parameters, including the cumulative number of Washington VAAC alerts, the height of the eruptive  
565 plumes did not (Fig. 8). A possible explanation for the similar plume heights could be that explosions were  
566 triggered by slugs of gas that reached a certain threshold (Woitischek et al. 2020). On the contrary, the high  
567 number of VAAC alerts is most likely associated to the increase of explosion frequency (given that there  
568 is more available gas), co-pyroclastic plumes triggered by various lava front collapses (Figs. 5d, 5f & 5h)  
569 and/or the intense erosion (lateral, vertical, and down- and upstream) of Volcano ravine at the southeastern  
570 flank.

571  
572 At Sangay, most of the thermal alerts are related to lava flow emplacement. In 2001-2013, the maximum  
573 time-average discharge rate (TADR) was 2.07 m<sup>3</sup>/s, in 2015 it reached 2.95 m<sup>3</sup>/s, in 2016: 5.65 m<sup>3</sup>/s, in  
574 2017: 5.16 m<sup>3</sup>/s, in 2018: 3.55 m<sup>3</sup>/s and in 2019-2020 it increased drastically to 21.8 m<sup>3</sup>/s (Table 1). Overall,  
575 from 2001 to 2013 max TADR was the lowest throughout the entire study period (Fig. 8e), which could be

576 related to the emptying of the shallow reservoir via minor but long-lasting (i.e. continuous) activity. In  
577 contrast, in the episodic period (2015-2018) there was an increase in max time-average discharge rate from  
578 2015 to 2016, while in 2017 it started to drop until 2018, forming a bell-shaped pattern (Fig. 5b & 8e). The  
579 2001-2018 period could be interpreted as starting with a steady-state reservoir, which fed the system from  
580 2001 to 2013. Then, between 2015 and 2018, second boiling and/or injections of new magma provided the  
581 necessary gas to trigger the episodic period that expelled the remaining magma of 2001-2013. Finally, the  
582 much higher max time-average discharge rate in 2019-2020 (Fig. 8e) is most likely related to a new  
583 voluminous and gas-rich injection of magma that ascended from depth, as was interpreted based on  
584 aforementioned monitoring parameters.

585  
586 Similar changes in the eruptive behavior from long-lasting to episodic eruptions have been reported for the  
587 long-term activity of other volcanoes (e.g., Tungurahua, Hidalgo et al. 2015). Nevertheless, a detailed  
588 comparison with other similar systems is not possible given the lack of continuous data on Sangay, as well  
589 as the lack of long-term research studies published for open-system volcanoes.

#### 590 591 **4.2. Model of magma discharge based on injection, cooling and viscous relaxation time relationship**

592  
593 Given the long-lasting activity recorded pre-2013 and since 2019, we can argue that a persistently  
594 replenished shallow magmatic reservoir must be feeding the surface eruptive activity under a steady-state  
595 behavior, similar to that observed at basaltic open systems like Stromboli and Etna (Wadge and Guest 1981;  
596 Harris and Stevenson 1997). The different intensity of the activity, which was mild pre-2013 and intense  
597 since 2019, could be controlled by the injection size and time. It seems that more voluminous basic and  
598 gas-rich magma intrusions with shorter injection times are responsible for the 2019-ongoing activity (Fig.  
599 8), making this phase last longer and show more intense surface activity than before. Steady-state behavior  
600 like the one observed during these two periods could be recurrent at Sangay, nevertheless, we only have  
601 insights into the last 20 years of activity.

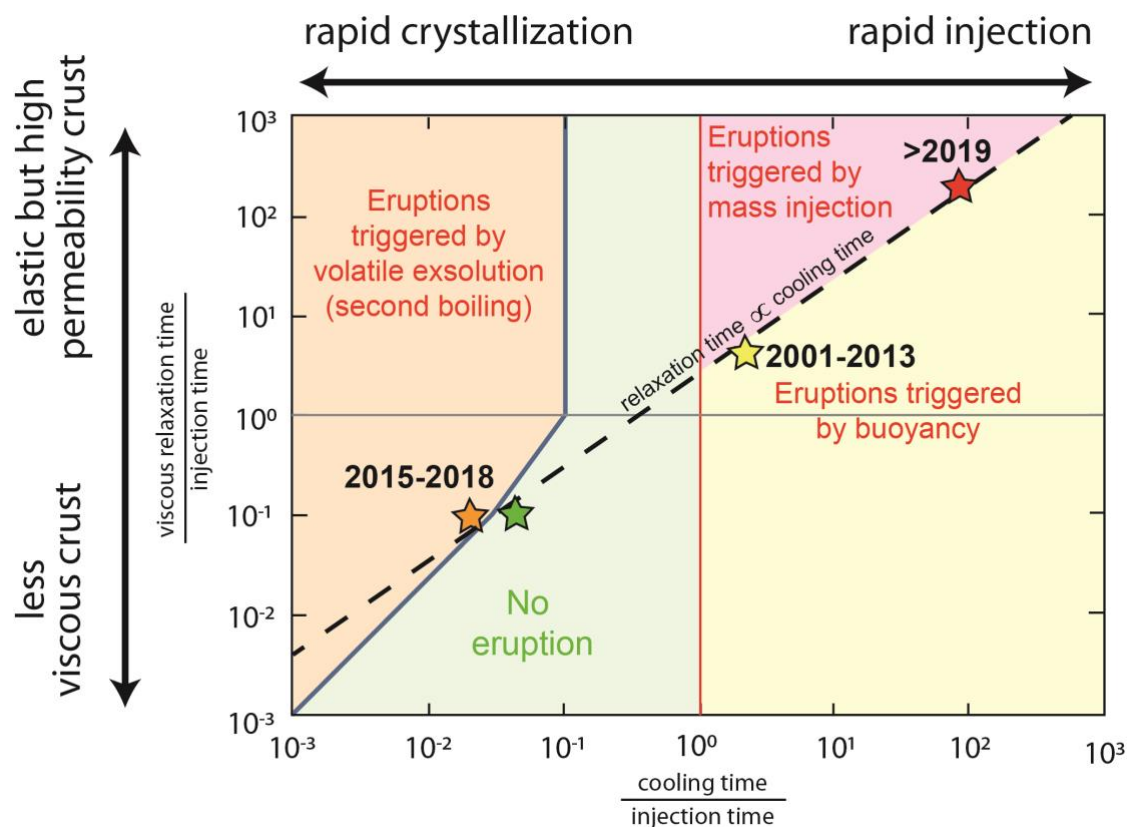
602  
603 In between these two long-lasting eruptive periods, for 4 years, from 2015 to 2018, Sangay displayed  
604 episodic activity of shorter duration and milder surface phenomena. Silica content seems to slightly evolve  
605 from more basic magmas sampled in the 1990s to a slightly more differentiated composition for 2015 and  
606 2018 (Fig. 8a). This could be in agreement with a progressive magma depletion and passive degassing of  
607 the shallow reservoir, followed by a crystallization induced heating and volatile exsolution of the upper  
608 remaining magma ending in eruption by second boiling (Wadge and Guest 1981; Tait et al. 1989; Putirka  
609 2017). Smaller intrusions could also have triggered the remaining slightly more differentiated magma to  
610 become eruptible again and produced the short duration episodes observed between 2015 and 2018.

611  
612 We propose a simplified model based on Degruyter and Huber (2014) and Mittal and Richards (2019) to  
613 explain the geophysical and subaerial observations from Sangay. The model defines characteristic  
614 timescales for different processes and depending on the ratios between them, different regimes occur, either  
615 locking the magma (no eruption) or leading to an eruption (eruptions triggered by second boiling, mass  
616 injections or buoyancy) (Fig. 9). The timescales, in the more general model, are related to: *magma injection*,  
617 *reservoir cooling*, *viscous relaxation of the crust*, *fluid pore pressure* and its *diffusion* (Degruyter and Huber  
618 2014; Mittal and Richards 2019). These parameters are calculated from structural and rheological properties  
619 of the magmatic system (e.g., magma density and viscosity, size of reservoir, length of conduit,  
620 permeability of crust, thermal and pore diffusivities, etc.), most of which are unknown for Sangay.  
621 However, the known surface activity, rest outgassing and/or erupting, can be used to locate any specific  
622 activity in Fig. 9 and propose a range of values for the ratio of timescales at this specific time. We assume  
623 that there were no significant changes over the last two decades regarding the geometry of the volcanic  
624 system as well as the viscous relaxation and cooling times. In this case, changes in the injection time,  
625 controlled by variations in magma inflow rate to the reservoir, result in a proportional change in the  
626 parameter space defined by relaxation to injection times vs. the cooling to injection times (Fig. 9).  
627 Moreover, the fact that gas emissions occurred even during periods when other variables remained low,  
628 indicates that the reservoir is open to degassing, i.e., that the system maintains a non-zero permeability  
629 (efficient volatile diffusion), resulting in a model that combines the Degruyter and Huber (2014) diagram  
630 and the third regime defined by Mittal and Richards (2019) for the evolution of Sangay's eruptive activity  
631 (Fig. 9).

632  
633 We hypothesize that the different eruptive periods observed at Sangay over the last years obey to different  
634 scaling between these timescales. For instance, if the geometry of the system remains unchanged, the rate  
635 of magma injection into the reservoir and/or changes in permeability would lead to transitions between the



636 various regimes (Fig. 9). The fact that the height of the ash plumes is confined to a narrow range over the  
 637 last 20 years suggests that the eruption style is similar throughout the different periods, while the frequency  
 638 of the events and duration of each eruptive phase stay variable. The simplest way to explain these variations  
 639 is to attribute the primary role in the dynamics to the rate of magma intrusion (i.e. magma injection time)  
 640 (Degruyter and Huber 2014; Mittal and Richards 2019). A decrease in the injection time due to an increase  
 641 in the mass inflow rate could lead to a situation in which the time for pore diffusion is much higher than  
 642 the time for magma intrusion. In both long-lasting periods, eruptions could have been triggered by mass  
 643 injection or by buoyancy (controlled by volatile content), depending on how efficient viscous relaxation of  
 644 the edifice was with respect to magma intrusion. Based on their different chemistry, volume and degassing,  
 645 the 2001-2013 eruptions were most likely fueled by buoyancy, while the 2019-ongoing ones probably result  
 646 from mass injection (Fig. 9). On the other hand, the episodic period between 2015 and 2018 could respond  
 647 to a lower mass inflow rate (i.e. higher injection time), due to which the system produced sporadic eruptions  
 648 by second boiling or remained quiet due to locking of the magma (Fig. 9). In all cases, the frequency of the  
 649 eruptions is directly related to the mass inflow rate, which is a way to understand the changes from episodic  
 650 to long-lasting activity at Sangay volcano.  
 651



652  
 653 **Fig. 9** Simplified conceptual model of the various regimes that control the evolution of eruptive activity based on  
 654 magma inflow rate into the reservoir and the relationship between injection, cooling and viscous relaxation times.  
 655 Modified from Degruyter and Huber (2014) and Mittal and Richards (2019). Black dashed line indicates the possible  
 656 trajectory in this model for Sangay eruptions throughout the last two decades, assuming negligible changes in the  
 657 geometry of the volcanic system, the viscous relaxation and cooling times.  
 658

## 659 5. CONCLUSION

660 Sangay is the most active volcano in continental Ecuador. For the last 20 years, we identified seven eruptive  
 661 phases clustered into three major eruptive periods based on ground-based and satellite-derived information.  
 662 These periods were of long-lasting (2001-2013 & 2019-ongoing) and episodic nature (2015, 2016, 2017 &  
 663 2018). Surface activity remained similar over time; eruptive columns reached  $1 \pm 0.6$  km above the crater  
 664 level and lava flows of 1-3 km length were emplaced towards the eastern and southeastern flanks and  
 665 frequently produced pyroclastic density currents due to lava front collapses. In contrast, magma  
 666 composition has become slightly more basic over time, shifting from 60.7 wt% in 2015 to 59.0 wt%  $\text{SiO}_2$   
 667 in 2020, indicating new magma injections.  
 668

669 Over the last 20 years, Sangay volcano has extruded at least  $326 \pm 163$  million  $\text{m}^3$  of magma in three main  
 670 periods. The first one emitted  $100 \pm 50$  million  $\text{m}^3$  through long-lasting activity. The second expelled  $54 \pm 27$

671 million m<sup>3</sup> in four short-lasting eruptive episodes, which lasted ~100 days each. Finally, the 2019-ongoing  
672 eruptive period has been the most intense one in the last two decades. It has extruded more than 172±86  
673 million m<sup>3</sup> (until 31 May 2020). The high discharge rate (TADR) in this period has triggered numerous  
674 lava front collapses (i.e., pyroclastic density currents) which have aggressively eroded Volcán ravine.  
675 Rainfall-triggered secondary lahars have at various times temporarily dammed the Upano river located 25  
676 km downstream, marking the first time in the last two decades that lahars have been reported and have  
677 affected populated areas.

679 All the recorded parameters are consistent with open-vent activity explained by a variation in the deeper  
680 magma inflow rate into the reservoir, assuming that structural and rheological properties of the magmatic  
681 system remain confined to a relatively narrow range during the study period. Observation of these changes  
682 would not have been possible without the long-term multi-parametric monitoring presented here. These  
683 techniques, if adopted elsewhere, have the potential to provide new insights into the “unpredictable”  
684 behavior of other andesitic open system volcanoes worldwide.

### 686 Acknowledgement

687 The first author thanks the late Luis Peña and Wilson Franco for their friendship and unconditional support  
688 to Vasconez family, which allowed them to begin and successfully end his educational career. The authors  
689 would like to thank the entire staff of ECU-911 Macas, in particular to Luis Castillo for gently sharing  
690 pictures and videos of Sangay eruptions. Special acknowledgment goes also to Byron Rivadeneira, Diego  
691 Barba, Jorge Anhalzer, Eric Brosier and Grupo Aéreo del Ejército Ecuatoriano for their cooperation in  
692 station maintenance. We also thank the entire staff of Instituto Geofísico of Escuela Politécnica Nacional  
693 (IG-EPN) in particular to Marco Antonio Solís, Jéssica Mejía, Paola Nazate, Luis Velez, Daniel Cárdenas,  
694 Sandro Vaca, Freddy Vásconez, Francisco Mejía, Iván Tapa, Ana Peralvo and Andrea Cordova. We also  
695 thank Pablo Samaniego, who gently shared the geochemistry data from Monzier et al., 1999. Finally, we  
696 thank the two anonymous reviewers and the editor for their insightful and constructive comments which  
697 helped to improve the original manuscript. Part of this investigation was funded thanks to the PAPIIT  
698 project IA102221. This research was conducted in the context of IG-EPN’s project “Generación de  
699 Capacidades para la Emisión de Alertas Tempranas” funded by Secretaría Nacional de Planificación y  
700 Desarrollo (SENPLADES) and the Laboratoire Mixte International Seismes et Volcans dans les Andes du  
701 Nord (LMI SVAN).

### 703 Data availability

704 Supporting information is available alongside the online version of this manuscript. Supplementary  
705 Material 1: Subspace detector and binary classifier and Supplementary Material 2: Geochemical data.

### 707 REFERENCES

- 708 Barrett SA, Beroza GC (2014) An empirical approach to subspace detection. *Seismological Research Letters* 85:594–600
- 709 Battaglia J, Hidalgo S, Bernard B, et al (2019) Autopsy of an eruptive phase of Tungurahua volcano (Ecuador) through  
710 coupling of seismo-acoustic and SO<sub>2</sub> recordings with ash characteristics. *Earth and Planetary Science Letters*  
711 511:223–232. <https://doi.org/10.1016/j.epsl.2019.01.042>
- 712 Battaglia J, Métaixian J-P, Garaebiti E (2016) Families of similar events and modes of oscillation of the conduit at Yasur  
713 volcano (Vanuatu). *Journal of Volcanology and Geothermal Research* 322:196–211
- 714 Bernard B, Encalada Simbaña M, Báez C, et al (2019) Dispersion of volcanic ash clouds in Ecuador: a 20 years perspective.  
715 In: Abstract volume of the 8th International Symposium on Andean Geodynamics. Quito, Ecuador
- 716 Carn SA, Krueger AJ, Arellano S, et al (2008) Daily monitoring of Ecuadorian volcanic degassing from space. *Journal of*  
717 *Volcanology and Geothermal Research* 176:141–150. <https://doi.org/10.1016/j.jvolgeores.2008.01.029>
- 718 Coppola D, Laiolo M, Cigolini C, et al (2016) Enhanced volcanic hot-spot detection using MODIS IR data: results from the  
719 MIROVA system. *Geological Society, London, Special Publications* 426:181–205. <https://doi.org/10.1144/SP426.5>
- 720 Coppola D, Laiolo M, Piscopo D, Cigolini C (2013) Rheological control on the radiant density of active lava flows and domes.  
721 *Journal of Volcanology and Geothermal Research* 249:39–48. <https://doi.org/10.1016/j.jvolgeores.2012.09.005>
- 722 Coppola D, Piscopo D, Staudacher T, Cigolini C (2009) Lava discharge rate and effusive pattern at Piton de la Fournaise from  
723 MODIS data. *Journal of Volcanology and Geothermal Research* 184:174–192.  
724 <https://doi.org/10.1016/j.jvolgeores.2008.11.031>
- 725 Coppola D, Ripepe M, Laiolo M, Cigolini C (2017) Modelling satellite-derived magma discharge to explain caldera collapse.  
726 *Geology* 45:523–526. <https://doi.org/10.1130/G38866.1>
- 727 Cotten J, Le Dez A, Bau M, et al (1995) Origin of anomalous rare-earth element and yttrium enrichments in subaerially  
728 exposed basalts: evidence from French Polynesia. *Chemical Geology* 119:115–138
- 729 De La Hoz C, Tary JB, Lomax A (2021) Empirical subspace detection applied to triggered seismicity by the July 25, 2011,  
730 Mw 5.0 earthquake in the Sea of Marmara, Turkey. *Computers & Geosciences* 104738
- 731 Degruyter W, Huber C (2014) A model for eruption frequency of upper crustal silicic magma chambers. *Earth and Planetary*  
732 *Science Letters* 403:117–130. <https://doi.org/10.1016/j.epsl.2014.06.047>
- 733 Global Volcanism Program (1976) Report on Sangay (Ecuador). Smithsonian Institution
- 734 Global Volcanism Program (1996) Report on Sangay (Ecuador). Smithsonian Institution
- 735 Hall ML (1977) El volcanismo en el Ecuador. IPGH, Sección Nacional del Ecuador

736 Harris AJL, Stevenson DS (1997) Magma budgets and steady-state activity of Vulcano and Stromboli. *Geophysical Research*  
737 *Letters* 24:4. <https://doi.org/10.1029/97GL00861>

738 Harris DB (2006) Subspace detectors: theory. Lawrence Livermore National Lab.(LLNL), Livermore, CA (United States)

739 Hedelt P, Efremenko DS, Loyola DG, et al (2019) Sulfur dioxide layer height retrieval from Sentinel-5 Precursor/TROPOMI  
740 using FP\_ILM. *Atmos Meas Tech* 12:5503–5517. <https://doi.org/10.5194/amt-12-5503-2019>

741 Hidalgo S, Battaglia J, Arellano S, et al (2015) SO<sub>2</sub> degassing at Tungurahua volcano (Ecuador) between 2007 and 2013:  
742 Transition from continuous to episodic activity. *Journal of Volcanology and Geothermal Research* 298:1–14.  
743 <https://doi.org/10.1016/j.jvolgeores.2015.03.022>

744 Humphreys MCS, Blundy JD, Sparks RSJ (2007) Shallow-level decompression crystallisation and deep magma supply at  
745 Shiveluch Volcano. *Contrib Mineral Petrol* 155:45–61. <https://doi.org/10.1007/s00410-007-0223-7>

746 IGEPN (2018) Special report N°2, Sangay: Continua el proceso eruptivo. [https://www.igepn.edu.ec/sangay-informes/sang-  
748 especiales/sang-e-2018/21713-informe-especial-sangay-n-2-21-11-2018/file](https://www.igepn.edu.ec/sangay-informes/sang-<br/>
747 especiales/sang-e-2018/21713-informe-especial-sangay-n-2-21-11-2018/file)

749 IGEPN (2020) Special report N°3, Sangay: Actualización de la actividad eruptiva. [https://www.igepn.edu.ec/sangay-  
751 informes/sang-especiales/sang-e-2020/24008-informe-especial-sangay-n-3-12-06-2020/file](https://www.igepn.edu.ec/sangay-<br/>
750 informes/sang-especiales/sang-e-2020/24008-informe-especial-sangay-n-3-12-06-2020/file). Accessed 2 Aug 2020

752 Johansson ME (2009) Application of passive DOAS for studies of megacity air pollution and volcanic gas emissions. Chalmers  
753 University of Technology

754 Johnson JB, Lees JM (2000) Plugs and chugs—seismic and acoustic observations of degassing explosions at Karymsky,  
755 Russia and Sangay, Ecuador. *Journal of Volcanology and Geothermal Research* 101:67–82.  
756 [https://doi.org/10.1016/S0377-0273\(00\)00164-5](https://doi.org/10.1016/S0377-0273(00)00164-5)

757 Konstantinou KI, Lin CH (2004) Nonlinear Time Series Analysis of Volcanic Tremor Events Recorded at Sangay Volcano,  
758 Ecuador. *Pure appl geophys* 161:19

759 Lees JM, Ruiz M (2008) Non-linear explosion tremor at Sangay, Volcano, Ecuador. *Journal of Volcanology and Geothermal*  
760 *Research* 176:170–178. <https://doi.org/10.1016/j.jvolgeores.2007.08.012>

761 Michaut C, Ricard Y, Bercovici D, Sparks RSJ (2013) Eruption cyclicity at silicic volcanoes potentially caused by magmatic  
762 gas waves. *Nature Geosci* 6:856–860. <https://doi.org/10.1038/ngeo1928>

763 Mittal T, Richards MA (2019) Volatile Degassing From Magma Chambers as a Control on Volcanic Eruptions. *J Geophys*  
764 *Res Solid Earth* 124:7869–7901. <https://doi.org/10.1029/2018JB016983>

765 Monzier M, Robin C, Samaniego P, et al (1999) Sangay volcano, Ecuador: structural development, present activity and  
766 petrology. *Journal of Volcanology and Geothermal Research* 90:49–79

767 Morales Rivera AM, Amelung F, Mothes P (2016) Volcano deformation survey over the Northern and Central Andes with  
768 ALOS InSAR time series: deformation survey over the Andes. *Geochem Geophys Geosyst* 17:2869–2883.  
769 <https://doi.org/10.1002/2016GC006393>

770 Naismith AK, Matthew Watson I, Escobar-Wolf R, et al (2019) Eruption frequency patterns through time for the current  
771 (1999–2018) activity cycle at Volcán de Fuego derived from remote sensing data: Evidence for an accelerating cycle  
772 of explosive paroxysms and potential implications of eruptive activity. *Journal of Volcanology and Geothermal*  
773 *Research* 371:206–219. <https://doi.org/10.1016/j.jvolgeores.2019.01.001>

774 Narvaez DF, Rose-Koga EF, Samaniego P, et al (2018) Constraining magma sources using primitive olivine-hosted melt  
775 inclusions from Puñalica and Sangay volcanoes (Ecuador). *Contributions to Mineralogy and Petrology* 173:.  
776 <https://doi.org/10.1007/s00410-018-1508-8>

777 Ordoñez J, Vallejo Vargas S, Bustillos JE, et al (2013) Volcán Sangay, peligros volcánicos potenciales

778 Ortiz HD, Matoza RS, Garapaty C, et al (2020) Multi-year regional infrasound detection of Tungurahua, El Reventador, and  
779 Sangay volcanoes in Ecuador from 2006 to 2013. *Acoustical Society of America, USA*, p 13

780 Peccerillo A, Taylor SR (1976) Geochemistry of Eocene calc-alkaline volcanic rocks from the Kastamonu area, northern  
781 Turkey. *Contributions to mineralogy and petrology* 58:63–81

782 Putirka KD (2017) Down the Crater: Where Magmas are Stored and Why They Erupt. *ELEMENTS* 13:11–16.  
783 <https://doi.org/10.2113/gselements.13.1.11>

784 Tait S, Jaupart C, Vergnolle S (1989) Pressure, gas content and eruption periodicity of a shallow, crystallising magma  
785 chamber. *Earth and Planetary Science Letters* 92:107–123. [https://doi.org/10.1016/0012-821X\(89\)90025-3](https://doi.org/10.1016/0012-821X(89)90025-3)

786 Theys N, Hedelt P, De Smedt I, et al (2019) Global monitoring of volcanic SO<sub>2</sub> degassing with unprecedented resolution from  
787 TROPOMI onboard Sentinel-5 Precursor. *Sci Rep* 9:2643. <https://doi.org/10.1038/s41598-019-39279-y>

788 Valade S, Ley A, Massimetti F, et al (2019) Towards Global Volcano Monitoring Using Multisensor Sentinel Missions and  
789 Artificial Intelligence: The MOUNTS Monitoring System. *Remote Sensing* 11:1528.  
790 <https://doi.org/10.3390/rs11131528>

791 Valverde V, Mothes P, Beate B, Bernard J (2021) Enormous and far-reaching debris avalanche deposits from Sangay volcano  
792 (Ecuador): Multidisciplinary study and modeling the 30 ka sector collapse. *Journal of Volcanology and Geothermal*  
793 *Research* 107172. <https://doi.org/10.1016/j.jvolgeores.2021.107172>

794 Villareal R (2017) Plan estratégico institucional del Gobierno Autónomo Descentralizado del cantón Morona. Gobierno  
795 Autónomo Descentralizado del cantón Morona, Macas

796 Wadge G, Guest JE (1981) Steady-state magma discharge at Etna 1971–81. *Nature* 294:548–550

797 Walter TR, Haghshenas Haghighi M, Schneider FM, et al (2019) Complex hazard cascade culminating in the Anak Krakatau  
798 sector collapse. *Nat Commun* 10:4339. <https://doi.org/10.1038/s41467-019-12284-5>

799 Wang W, Cao C, Bai Y, et al (2017) Assessment of the NOAA S-NPP VIIRS Geolocation Reprocessing Improvements.  
800 *Remote Sensing* 9:974. <https://doi.org/10.3390/rs9100974>

801 Woitischek J, Edmonds M, Woods AW (2020) The control of magma crystallinity on the fluctuations in gas composition at  
open vent basaltic volcanoes. *Scientific Reports* 10:8. <https://www.nature.com/articles/s41598-020-71667-7>